

Ly α Emitters at $z = 5.7$ in the Subaru Deep Field ^{*,†}

Kazuhiro SHIMASAKU, ^{1,2} Nobunari KASHIKAWA, ^{3,4} Mamoru DOI, ^{5,2} Chun LY, ⁶
Matthew A. MALKAN, ⁶ Yuichi MATSUDA, ⁷ Masami OUCHI, ^{8,‡}
Tomoki HAYASHINO, ⁹ Masanori IYE, ^{3,4} Kentaro MOTOHARA, ⁵ Takashi MURAYAMA, ¹⁰
Tohru NAGAO, ^{3,11} Kouji OHTA, ¹² Sadanori OKAMURA, ^{1,2} Toshiyuki SASAKI, ¹³
Yasuhiro SHIOYA, ¹⁰ Yoshiaki TANIGUCHI ¹⁰

¹*Department of Astronomy, School of Science, The University of Tokyo, Tokyo 113-0033*
Email (KS): shimasaku@astron.s.u-tokyo.ac.jp

²*Research Center for the Early Universe, School of Science, The University of Tokyo,*
Tokyo 113-0033

³*Optical and Infrared Astronomy Division, National Astronomical Observatory, Mitaka,*
Tokyo 181-8588

⁴*Department of Astronomy, School of Science, Graduate University for Advanced Studies,*
Mitaka, Tokyo 181-8588

⁵*Institute of Astronomy, School of Science, The University of Tokyo, Mitaka 181-0015*

⁶*Department of Astronomy, University of California at Los Angeles, Los Angeles,*
CA 90095-1547, USA

⁷*Department of Astronomy, Graduate School of Science, Kyoto University, Kyoto 606-8502*

⁸*Space Telescope Science Institute, 3700 San Martin Drive, Baltimore, MD 21218, USA*

⁹*Research Center for Neutrino Science, Graduate School of Science, Tohoku University,*
Aramaki, Aoba, Sendai 980-8578

¹⁰*Astronomical Institute, Graduate School of Science, Tohoku University, Aramaki, Aoba,*
Sendai 980-8578, Japan

¹¹*INAF / Osservatorio Astrofisico di Arcetri Largo E. Fermi 5, 50125 Firenze, Italy*

¹²*Kouji Ohta Department of Astronomy, Kyoto University, Kyoto 606-8502*

¹³*Subaru Telescope, National Astronomical Observatory of Japan, 650 N. A'ohoku Place,*
Hilo, HI 96720, USA

(Received 2005 October 26; accepted 2006 February 27)

Abstract

We present the properties of Ly α emitters (LAEs) at $z = 5.7$ in the Subaru Deep Field. A photometric sample of 89 LAE candidates is constructed from narrow-band (NB816) data down to $NB816 = 26.0$ (AB) in a continuous 725 arcmin² area. Spectra of 39 objects satisfying the photometric selection criteria for LAEs were obtained with Subaru and Keck II Telescopes, among which 28 were confirmed LAEs, one was a nearby galaxy, and eight were unclassified. We also obtained spectra of another 24 NB816-excess objects in the field, identifying six additional LAEs. We find that the Ly α luminosity function derived from the photometric sample is reproduced well by a Schechter function with $L^* = 7.9^{+3.0}_{-2.2} \times 10^{42}$ erg s⁻¹ and $\phi^* = 6.3^{+3.0}_{-2.0} \times 10^{-4}$ Mpc⁻³ for $\alpha = -1.5$ (fixed) over the whole luminosity range of $L \simeq 3 \times 10^{42} - 3 \times 10^{43}$ erg s⁻¹. We then measure rest-frame Ly α equivalent widths (EWs) for the confirmed LAEs, to find that the median among the 28 objects satisfying the photometric selection criteria is $W_0^i = 233$ Å. We infer that 30% – 40% of LAEs at $z = 5.7$ exceed $W_0^i = 240$ Å. These large-EW objects probably cannot be accounted for by ordinary star-forming populations with a Salpeter IMF. We also find that LAEs with fainter far-UV luminosities have larger EWs. Finally, we derive the far-UV luminosity function of LAEs down to $M_{UV} \simeq -19.6$ using the photometric sample, and compare it with that of Lyman-break galaxies (LBGs). We find that as high as about 80% of LBGs at $z \sim 6$ have $W_0^i \geq 100$ Å, in sharp contrast to lower- z counterparts.

Key words: galaxies: evolution — galaxies: high-redshift — galaxies: luminosity function, mass function — galaxies: photometry

1. Introduction

Ly α emitters (LAEs) are commonly seen in the high-redshift universe. Most of them are thought to be very young star-forming galaxies, although some may have an active nucleus and some could be primeval galaxies in a gas cooling phase before onset of the initial star formation or in superwind phases just after the initial star formation. The high number density of LAEs, roughly comparable to that of Lyman-break galaxies (LBGs), suggests that they are important in understanding the early evolution of galaxies.

LAEs at $z > 5$ are of particular interest in galaxy formation and cosmology, since they are not only expected to be extremely young but also an invaluable probe of the universe during or just after reionization. They can be used to infer the reionization epoch of the universe via the change in their number density (Haiman & Spaans 1999; Rhoads & Malhotra 2001; Haiman 2002; Malhotra & Rhoads 2004; Stern et al. 2005; Kashikawa et al. 2005). However, although there has been rapid progress in the observation of LAEs at $z > 5$ (e.g., Rhoads & Malhotra 2001; Ajiki et al. 2003, 2004; Kodaira et al. 2003; Hu et al. 2002, 2004; Maier et al. 2003; Rhoads et al. 2003; Ouchi et al. 2005; Taniguchi et al. 2005), the data obtained to date are not sufficient to place strong constraints on their fundamental properties such as the luminosity function (LF), in contrast to the data of LBGs at similar redshifts. Usually, narrow-band surveys are used to detect LAEs. Their apparent faintness in both narrow bands (i.e., Ly α) and broad bands (off Ly α), as well as a small survey volume defined by the wavelength coverage of the narrow-band filter times the survey area, makes it difficult to obtain a large sample. Samples from several small surveys by different workers could be combined to form a larger sample. However, since the selection criteria of LAEs and the survey depth differ among the surveys, LFs calculated from such combined samples may have systematic uncertainties difficult to control.

In this paper, we report on the results of a very deep survey of LAEs at $z = 5.7$ in a wide, continuous area of 725 arcmin². The survey uses deep imaging data in six optical bandpasses including the narrow band NB816 ($\lambda_c = 8150$ Å and FWHM = 120 Å) targeted at the Ly α emission at $z \simeq 5.7 \pm 0.05$. All of the imaging data were taken with the Suprime-Cam (Miyazaki et al. 2002) at the Subaru Telescope (Iye et al. 2004). From these data, we construct

a sample of 89 photometrically selected LAEs down to NB816 = 26.0. By followup spectroscopy with the Subaru and Keck II Telescopes, we obtained a sample of 34 LAEs with confirmed redshifts.

Combining these samples with Monte Carlo simulations, we calculate the Ly α LF, which is the most reliable measurement for the LF of $z = 5.7$ LAEs published to date. This LF serves as a ‘zero point’ for the LF in the fully ionized universe ($z < 6$), which is to be compared with the LF at $z > 6$ to probe the reionization history of the universe. A companion paper (Kashikawa et al. 2005) compares the LF at $z = 5.7$ obtained in this paper with that for $z = 6.5$ LAEs, and discusses the ionization state of the intergalactic medium at $z = 6.5$.

We also derive accurately the far UV continuum LF and the distribution of Ly α equivalent widths (EWs), both of which have not yet been strongly constrained for LAEs at $z > 5$. Comparing the far UV LF of our LAEs with that of LBGs at $z \sim 6$ given in the literature, we examine what fraction of LBGs have EWs large enough to be detected as LAEs, and discuss evolution of Ly α properties of star-forming galaxies.

The plan of this paper is as follows. Section 2 describes the photometric and spectroscopic data used in this study. The confirmed sample of 34 LAEs is constructed in §3. The photometric selection of LAEs is made in §4. Section 5 is devoted to results and discussion, and a summary is given in §6. AB magnitudes are used in this paper. We assume a flat universe with $\Omega_M = 0.3$, $\Omega_\Lambda = 0.7$, and $H_0 = 70$ km s⁻¹ Mpc⁻¹.

2. Data

2.1. Imaging Data

The SDF has deep, public Subaru/Suprime-Cam data in seven bandpasses, B , V , R , i' , z' , NB816, and NB921, obtained for the Subaru Deep Field Project (Kashikawa et al. 2004; see also Maihara et al. 2001 for the Subaru Deep Field). This project is a large program of Subaru Observatory to carry out a deep galaxy survey in a blank field in optical and NIR wavelengths to study distant galaxies. B , V , R , i' , and z' are standard Johnson and SDSS broad bands, and NB816 and NB921 are narrow bands whose central wavelength and FWHM are (8150 Å, 120 Å) and (9196 Å, 132 Å), respectively. In this paper, we use the B , V , R , i' , z' , and NB816 data to study LAEs at $z = 5.7$. The exposure times and the 3σ limiting magnitudes on a 2'' aperture are: 595 min and 28.45 mag (B), 340 min and 27.74 mag (V), 600 min and 27.80 mag (R), 801 min and 27.43 mag (i'), 504 min and 26.62 mag (z'), 600 min and 26.63 mag (NB816). These images have been convolved to a seeing of 0.''98 (FWHM) and an identical sky coverage of 29.''7 \times 36.''7. The pixel scale of the images is 0.''202 pixel⁻¹. The selection of $z = 5.7$ LAEs is made in the $R - z'$ vs $i' - \text{NB816}$ plane, and the B and V data are also used to further remove foreground objects.

Object detection and photometry were made using SExtractor version 2.1.6 (Bertin & Arnouts 1996) on all six images. The NB816-band image was chosen to de-

* Based on data collected at the Subaru Telescope, which is operated by the National Astronomical Observatory of Japan.

† Part of the data presented herein were obtained at the W.M. Keck Observatory, which is operated as a scientific partnership among the California Institute of Technology, the University of California and the National Aeronautics and Space Administration.

The Observatory was made possible by the generous financial support

of the W.M. Keck Foundation.

‡ Hubble Fellow.

tect objects. If more than 5 pixels whose counts were above the $2\sigma_{\text{sky}}$ were connected, they were regarded as an object. In total, 82,212 objects were detected down to the 3σ limiting magnitude of NB816. For each object detected in the NB816 image, a $2''$ -diameter magnitude was measured for each passband to derive the colors of each object. We adopted MAG_AUTO for the total NB816 magnitude. All the observed magnitudes and colors are corrected for Galactic absorption using the dust maps of Schlegel, Finkbeiner, & Davis (1998).

2.2. Spectra with FOCAS and DEIMOS

We made spectroscopic observations of 63 objects selected from the NB816-detected catalog with FOCAS (Kashikawa et al. 2002) on the Subaru Telescope and DEIMOS (Faber et al. 2003) on the Keck II Telescope. All 63 objects are NB816-excess objects with $i' - \text{NB816} \geq 1.0$ and $\text{NB816} \leq 26.0$. We first assigned slitlets to objects either with $R - z' \geq 1.0$ or undetected in R ; they are likely LAE candidates. We then included objects irrespective of $R - z'$ color in the target list if slitlets were available, in order to evaluate the completeness and contamination of the color-selected sample of LAE candidates to be constructed in Section 4.

2.2.1. FOCAS Spectroscopy

A total of 39 objects were observed with FOCAS in 2002 and 2004 in the multi-slit mode. Among them, three objects were observed on UT 2002 June 7 and 9 with a 300 lines mm^{-1} grating and an O58 order-cut filter using two masks. The typical spectral coverage was 5400 \AA – 10000 \AA with a pixel scale of 0.10 \AA pixel^{-1} . The use of 0.''8 slits gave a resolution of 9.5 \AA at 8150 \AA . The spatial resolution was 0.''3 pixel^{-1} by 3-pixel on-chip binning. The integration time per mask was 12600 seconds. The sky condition was good with a seeing size of 0.''4 – 1.''0. We also obtained spectra of the standard stars Hz 44 and Feige 34 for flux calibration. The data were reduced in a standard manner.

The remaining 36 objects were observed on UT 2004 April 24–27 with the same type of grating and order-cut filter. Six masks were used in total. The use of 0.''6 slits gave a resolution of 7.1 \AA at 8150 \AA . The spatial resolution was 0.''3 pixel^{-1} by 3-pixel on-chip binning. The integration time per mask was 12000–16800 seconds. The sky condition was good with a seeing size of 0.''4 – 0.''8. The standard stars Hz 44 and Feige 34 were observed for flux calibration. The data were reduced in a standard manner.

2.2.2. DEIMOS Spectroscopy

Twenty-four objects among the 63 were observed with DEIMOS on UT 2004 April 23 and 24. We used four MOS masks with an 830 line mm^{-1} grating and a GG495 order-cut filter. The spectral coverage was $\sim 5000 \text{ \AA} - 10000 \text{ \AA}$, with a central wavelength of 7500 \AA for one MOS mask and 8100 \AA for the other three. The slit width was 1.''0, giving a spectral resolution of 3.97 \AA . The integration times of individual masks were 7000 – 9000 seconds,

and the typical seeing sizes were 0.''55 – 1.''0. Spectra of the standard stars BD+28d4211 and Feige 110 were taken for flux calibration. The data were reduced with the spec2d pipeline.¹

3. Spectroscopic Sample of $z = 5.7$ LAEs

3.1. Classification of Spectra by Weighted Skewness

We classify the 63 objects with spectroscopic observations into LAEs and nearby emission-line objects using the features of emission lines. NB816-excess objects can be either nearby emitters ($\text{H}\alpha$, or $[\text{OIII}]$, or $[\text{OII}]$ emitters), or LAEs at $z \simeq 5.7$. Typically, the $\text{Ly}\alpha$ emission lines of high-redshift galaxies are single, asymmetric lines, with the profile blueward of 1216 \AA erased almost completely by neutral hydrogen gas. Thus, they can be discriminated from nearby emission lines, which are either single, symmetric lines, or doublet lines.

Objects with doublet emission lines are easy to classify; they are either $[\text{OII}]$ or $[\text{OIII}]$ emitters depending on the separation of the doublet lines. Objects with single emission lines are either LAEs, or $\text{H}\alpha$ emitters, or $[\text{OII}]$ emitters with unresolved doublet lines. To classify single emission-line objects, we introduce weighted skewness, S_W , which quantifies the asymmetry of emission lines. A similar quantity (skewness) has been applied by Kurk et al. (2004) to identify an LAE at $z = 6.518$.

For a given one-dimensional spectrum of an emission line, $f(x_i)$ ($i = 1, 2, \dots, n$), where x_i is the i -th pixel along wavelength and $f(x_i)$ is the flux in the i -th pixel, the weighted skewness is defined as

$$S_W = (\lambda_{10,r} - \lambda_{10,b}) \times \frac{1}{I\sigma^3} \sum_{i=1}^n (x_i - \bar{x})^3 f(x_i). \quad (1)$$

Here, $I = \sum f(x_i)$; $\bar{x} = \frac{1}{I} \sum x_i f(x_i)$; $\sigma = \sqrt{\frac{1}{I} \sum (x_i - \bar{x})^2 f(x_i)}$; $\lambda_{10,r}$ and $\lambda_{10,b}$ are the wavelengths where the flux drops to 10% of its peak value at the red and blue sides of the emission, respectively. In the above formula, $\frac{1}{I\sigma^3} \sum_{i=1}^n (x_i - \bar{x})^3 f(x_i)$ measures the skewness of the line, and $\lambda_{10,r} - \lambda_{10,b}$ measures the width of the line. Since the $\text{Ly}\alpha$ emission of high-redshift galaxies tends to be wider than other emission lines of nearby galaxies in the observed frame, we include the factor $\lambda_{10,r} - \lambda_{10,b}$ in S_W to enhance the difference between $\text{Ly}\alpha$ and other lines. S_W is larger for objects with higher asymmetries and/or larger line widths. Note that for an identical object, spectroscopy with a higher dispersion generally gives a larger S_W value. A full description of S_W is found in Kashikawa et al. (2005).

$\text{Ly}\alpha$ emission lines at high redshifts typically have large positive S_W values. On the other hand, $[\text{OIII}]$ and $\text{H}\alpha$ lines are nearly symmetric, i.e., $S_W \simeq 0$. The S_W of $[\text{OII}]$ emitters is also expected to be small (S_W is measured for the doublet as a whole); for all resolved $[\text{OII}]$ emitters in our sample, the $\lambda 3726$ line is weaker than the $\lambda 3729$ line,

¹ This pipeline was developed at UC Berkeley with support from NSF grant AST-0071048.

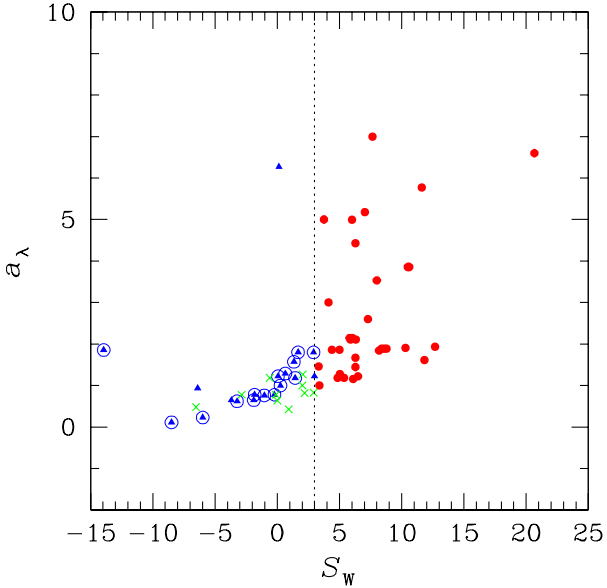


Fig. 1. Weighted skewness of the 63 objects with spectroscopic observations. The red circles, blue triangles, and green crosses indicate LAEs, nearby objects, and unclear objects, respectively. The objects with open blue circles have multiple emission lines. Ordinate shows wavelength ratio, a_λ .

meaning a negative S_W (See also Rhoads et al. 2003). This means that S_W can discriminate LAEs from [OII] emitters even when the [OII] doublet is not resolved in a spectrum due to a low spectral resolution and/or a low signal-to-noise ratio.

Figure 1 plots S_W for the 63 objects. The ordinate represents, for a reference, the wavelength ratio (a_λ) defined by Rhoads et al. (2003); a_λ is defined as $a_\lambda = (\lambda_{10,r} - \lambda_p) / (\lambda_p - \lambda_{10,b})$, where λ_p is the wavelength of the peak flux density. A loose correlation is found between a_λ and S_W in Fig. 1. Objects marked by a large open circle are nearby emitters with definite classification based on their emission lines; they are either H α emitters (from the presence of the [OIII] line or from a very flat and strong continuum over the whole wavelength range), or [OIII] emitters (from doublet lines at 4959 Å and 5007 Å), or [OII] emitters (from doublet lines at 3726 Å and 3729 Å). All these nearby objects have $S_W < 3$. A visual inspection of the 63 spectra reveals that most of the objects with $S_W > 3$ have an asymmetric emission-line shape typical of high-redshift Ly α emission.

On the basis of these results, we classify the spectroscopic objects into three classes as follows. We primarily use S_W , but in some cases we also use B and V photom-

etry as additional information, since LAEs at $z = 5.7$ are essentially invisible in our B and V data due to strong absorption by the IGM. If an object has the definite feature of the [OII] or [OIII] or H α line, it is a nearby object. If an object has a single emission-line with $S_W > 3$, it is regarded as an LAE (irrespective of the B and V fluxes); we assume that those with detected B or V fluxes are contaminated by a faint foreground object. If, on the other hand, a single-line object with $S_W < 3$ is detected in either B or V (i.e., brighter than the 2σ limit in the corresponding bandpass), then it is classified as a nearby object. Objects which do not satisfy either of the above three categories are classified as ‘unclear’ objects; unclear objects are single-line emitters with $S_W < 3$ but invisible in both B and V . Among the 63 objects, 34, 19, and 10 are classified as LAEs, nearby objects, and unclear objects. Among the 34 LAEs, six are detected in either B or V . This rather high contamination rate, $6/34 = 18\%$, appears to be accounted for by the observed surface number density of faint B/V sources. We find that the fraction of the sky occupied by faint ($m > 26$) B/V sources is about 10%. Furthermore, the probability of a faint B/V source being within $1''$ of a random position in the sky is found to be about 20%. The contamination rate obtained for the spectroscopic sample may be compared to these rough estimates of chance projection.

Table 1 summarizes the photometry and spectroscopy of the 63 objects. Figures 2 – 4 show the spectra of the LAEs, nearby objects, and unclear objects, respectively. The luminosity functions and star formation properties of the line-emitting galaxies at $z \lesssim 1.2$ identified in our spectroscopy will be discussed in Ly et al. (2006, in preparation).

We infer that some portion of the unclear objects may be LAEs in reality. This is because (i) not all LAEs may have as large asymmetry as the confirmed LAEs and (ii) since the resolution of the FOCAS spectra is significantly poorer than that of the DEIMOS spectra, the absolute value of S_W of an object based on a FOCAS spectrum will be smaller than that based on a DEIMOS spectrum. In this sense, the criterion of $S_W > 3$ is conservative in terms of the selection of LAEs. Among the ten unclear objects, eight are FOCAS objects. When estimating the selection completeness of the photometric sample of $z = 5.7$ LAEs in Section 4, we take account of the extreme possibility that all of the unclear objects are actually LAEs.

Figure 5 shows the distributions of emission-line wavelengths (the central value if the emission is a doublet) for all of our objects. The thick solid histogram in panel (a) represents the distribution for the 34 LAEs, and panel (b) plots the distributions for nearby objects (thin solid histogram) and unclear objects (dotted histogram). In both panels, the dashed curve corresponds to the response function of the NB816 band. It is found that while the distributions of nearby and unclear objects are statistically consistent with being symmetric around the central wavelength of the bandpass, the LAEs’ distribution is skewed toward shorter wavelengths. A natural explanation for this skewed distribution is as follows. LAEs with higher

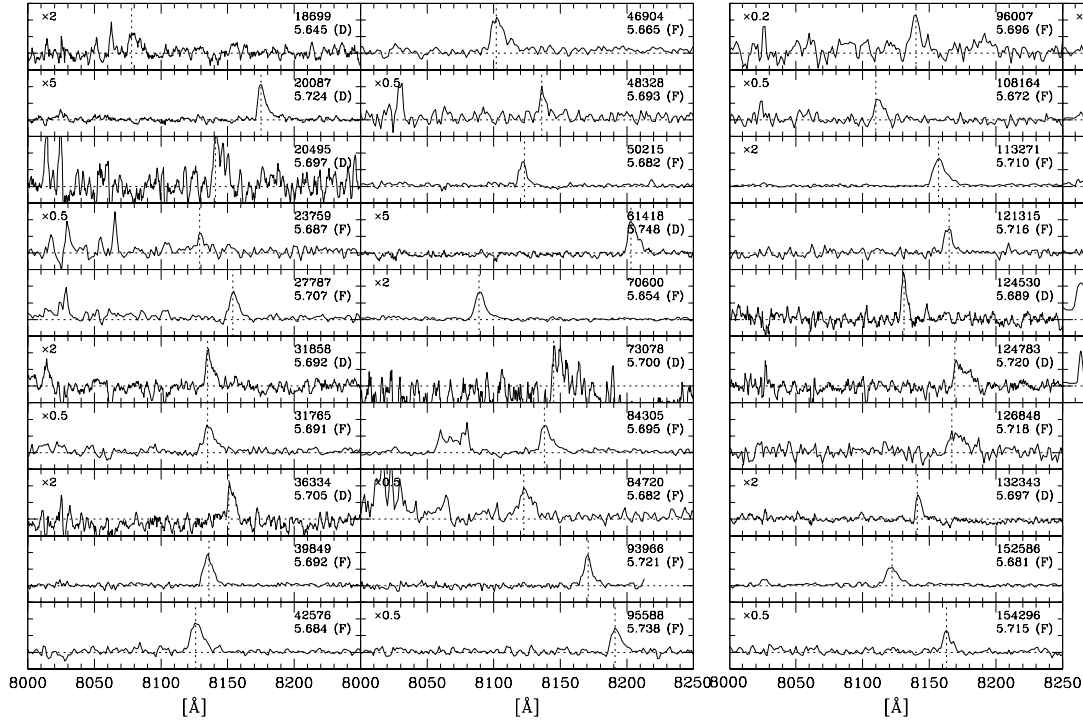


Fig. 2. Spectra of LAEs. The ID number (in the NB816-detected catalog) and redshift are shown in the upper right corner of each panel. ‘F’ (‘D’) in parentheses indicates that the object was observed with FOCAS (DEIMOS). The vertical dotted lines indicate the center of the (single) emission line. The scale on the y axis is marked in $0.5 \times 10^{-18} \text{ erg s}^{-1} \text{ cm}^{-2} \text{ Å}^{-1}$; for panels in which a factor is shown in the upper left corner, multiply the scale by this factor to obtain a correct scale.

redshifts are on average fainter in NB816 (even when the Ly α luminosity is fixed) because of a lower fraction of the continuum emission redward of $\lambda_{\text{rest}} = 1216 \text{ Å}$ falling into the NB816 bandpass. Hence they tend to be excluded from a list of spectroscopic targets.

The dotted curve in panel (a) represents the distribution of modeled LAEs with $\text{NB816} \leq 26.0$ in a mock sample; this sample is constructed based on the same selection criteria as for the observed sample (see the next section) from a large catalog of LAEs generated by Monte Carlo simulations for a range of LAE equivalent widths and luminosity function parameters (see Section 5). In the simulations, LAEs are distributed uniformly in comoving space over the redshift range $5.6 < z < 5.8$, which corresponds to an observed Ly α wavelength of 8020 to 8270 Å. The thick histogram is found to agree fairly well with the dotted curve, suggesting that prominent large-scale structures along the line of sight are not present in our LAE sample.

Hu et al. (2004) also found a skewed distribution in their $z = 5.7$ LAEs selected from NB816 data in the SSA22 field, and argued that the true center in wavelength of the NB816 filter may be shifted toward shorter wavelengths by about 25 Å than the measured one. Although we can-

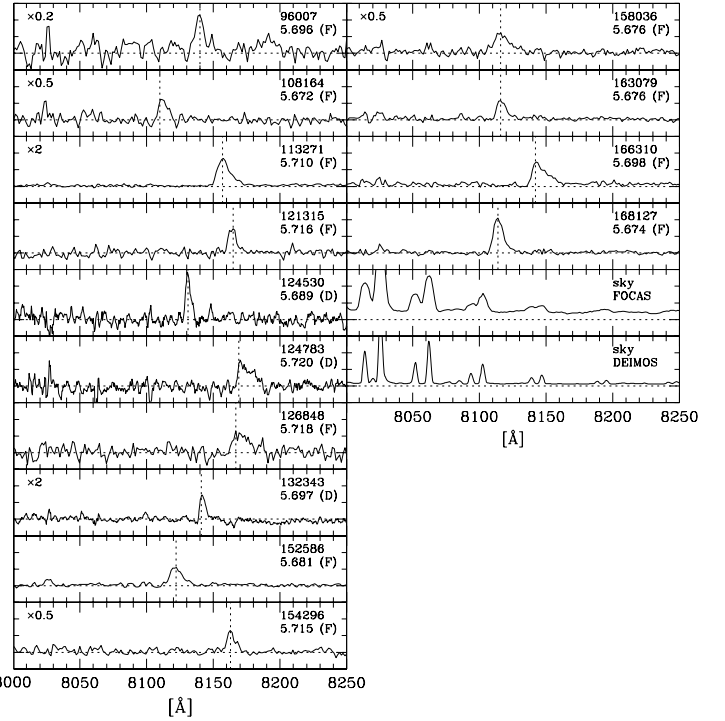


Fig. 2. Fig. 2 – continued. The second bottom and bottom panels in right-hand side show typical spectra of the sky background obtained with FOCAS and DEIMOS, respectively. The normalization is arbitrary.

not completely rule out this possibility, the wavelength distribution of our sample is explained without assuming such a shift.

3.2. Confirmed Sample of $z = 5.7$ LAEs

We have 34 LAEs with spectroscopic confirmation. Their distribution in the $i' - \text{NB816}$ vs NB816 plane is slightly biased toward brighter NB816 magnitudes and redder $i' - \text{NB816}$ colors with respect to the photometric sample, except for three objects of $i' - \text{NB816} \simeq 1.2$. Among the 34 objects, the faintest in NB816 is 25.89 mag.

We measure the flux and FWHM of the Ly α line from the spectrum of each object. In this paper, however, we adopt for Ly α fluxes the values calculated from the imaging data by subtracting the continuum flux measured from the z' -band image from the flux falling into the NB816 band, assuming $f_{\nu} = \text{constant}$; spectroscopic redshifts are used to determine the precise position of the Ly α line in the NB816 response function. The reason for not using the Ly α fluxes directly is that our multi-slit spectroscopy probably lost a non-negligible amount of Ly α photons, because of the relatively narrow slitlets (0."6 and 0."8 for FOCAS and 1."0 for DEIMOS) compared with the typical PSF sizes, and because the Ly α emission could be extended spatially. Figure 6 shows Ly α luminosities measured from the spectra against those from photometry (See Subsection 5.2 for the calculation of Ly α luminosities based on the photometric data). While lit-

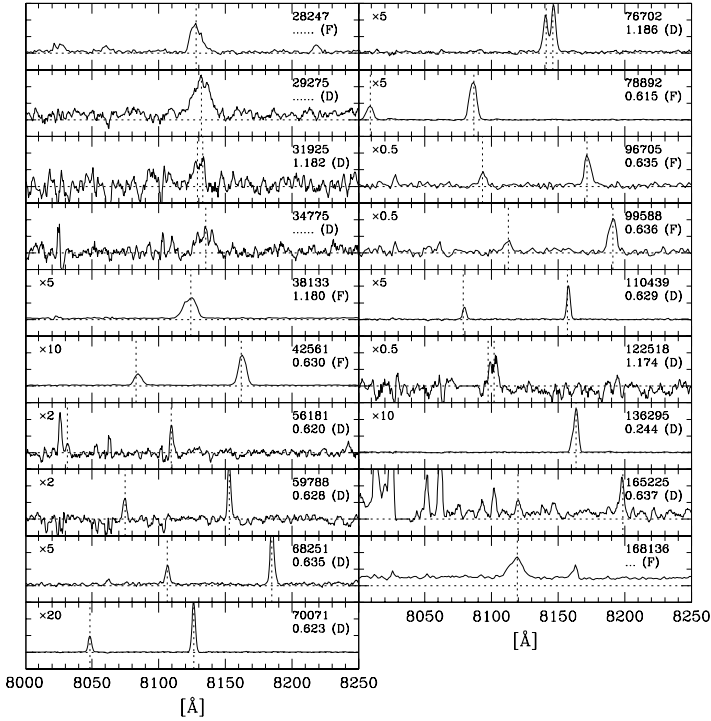


Fig. 3. Spectra of nearby objects. The ID number (in the NB816-detected catalog) and redshift are shown in the upper right corner of each panel. ‘F’ (‘D’) in parentheses indicates that the object was observed with FOCAS (DEIMOS). The vertical dotted lines indicate the identified emission lines ($H\alpha$ or $[OIII]$ or $[OII]$). Identification are unsuccessful for #28247, #29275, #34775, and #168136; these are classified as nearby objects because of a small skewness ($S_W < 3$) and a bright B or V magnitude. The scale on the y axis is marked in $1 \times 10^{-18} \text{ erg s}^{-1} \text{ cm}^{-2} \text{ \AA}^{-1}$; for panels in which a factor is shown in the upper left corner, multiply the scale by this factor to obtain a correct scale.

tle systematic difference is seen between the luminosities from the DEIMOS spectra and from the photometry, the FOCAS spectra give luminosities only about one third those measured from the photometric data. Among the FOCAS objects, three were observed with a $0.8''$ slitlet, and their $L(\text{Ly}\alpha(\text{spec}))/L(\text{Ly}\alpha(\text{phot}))$ ratio is 70% on average. These results are qualitatively consistent with narrower slitlets losing a larger fraction of $\text{Ly}\alpha$ photons. It is difficult to correct $L(\text{Ly}\alpha(\text{spec}))$ for this effect, since the seeing size varied during the exposures and since different objects have different intrinsic sizes. For the same reason, we also measure the equivalent widths of the 34 objects from the photometric data, as described in Subsection 5.2.

4. Photometric Sample of $z = 5.7$ LAEs

We construct a photometrically selected LAE sample from the imaging data. Objects located in low-quality regions of the images are excluded from the selection process to obtain an LAE sample of uniform detection. The low-quality regions include areas around very bright stars, the four edges of the images, and the south-east region

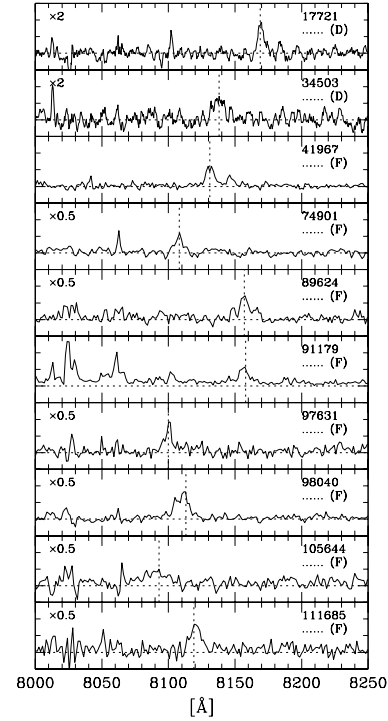


Fig. 4. Spectra of unclear objects. The ID number (in the NB816-detected catalog) is shown in the upper right corner of each panel. ‘F’ (‘D’) in parentheses indicates that the object was observed with FOCAS (DEIMOS). The vertical dotted lines indicate the position of the single emission line. The scale on the y axis is marked in $0.5 \times 10^{-18} \text{ erg s}^{-1} \text{ cm}^{-2} \text{ \AA}^{-1}$; for panels in which a factor is shown in the upper left corner, multiply the scale by this factor to obtain a correct scale.

which corresponds to the field of view of the CCD whose quantum efficiency is only about two thirds those of the other nine CCDs. The effective area is thus reduced to 725 arcmin^2 .

Figure 7 plots $i' - \text{NB816}$ color against NB816 magnitude for all objects with $\text{NB816} \leq 26.0$ ($N = 61,919$). The vast majority of the objects are distributed around $i' - \text{NB816} \sim 0.2$; their $i' - \text{NB816}$ distribution spreads as NB816 magnitude goes fainter, mainly due to the increase in photometric errors. Objects with large $i' - \text{NB816}$ colors are emission-line objects (or some kind of late-type stars with $i' - \text{NB816} > 1$), part of which are LAEs at $z = 5.7$. The large symbols indicate objects with spectroscopic observations: red circles, blue triangles, and green crosses indicate LAEs ($N = 34$), nearby objects (19), and unclear objects (10), respectively. For LAEs, open circles mean R magnitudes fainter than the 2σ magnitude ($N = 29$). The magenta line shows the threshold of $i' - \text{NB816}$ adopted for the selection of LAEs: $i' - \text{NB816} \geq 1.5$ (see below). The dotted line implies the i' -band 2σ magnitude. The i' -band magnitudes of objects undetected in i' (i.e., fainter than the 2σ magnitude) have been replaced with the 2σ magnitude.

Figure 8 shows the distribution of objects in the $R - z'$

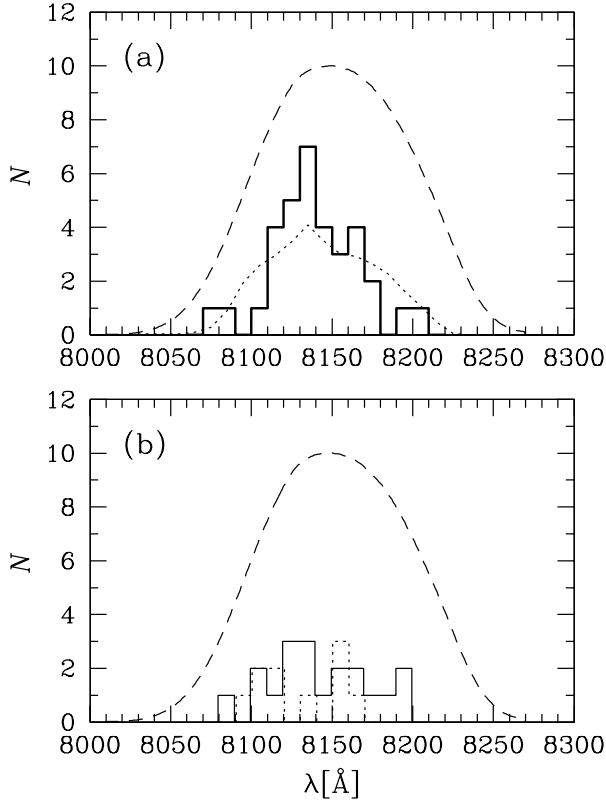


Fig. 5. Distributions of emission line wavelengths for objects with spectroscopic observations. *Panel (a).* The distribution for the 34 LAEs is shown by the thick solid histogram. *Panel (b).* The distributions for the 19 nearby objects (thin solid histogram) and the 10 unclear objects (dotted histogram). The dotted curve in panel (a) represents the distribution of model LAEs with $NB816 \leq 26.0$ in a mock sample (See text). In both panels, the dashed curve corresponds to the response function of the NB816 band.

vs $i' - NB816$ plane. In this figure, if an object is undetected (i.e., fainter than the 2σ magnitude) in a given bandpass, its magnitude in that bandpass is replaced with the 2σ magnitude. Objects on the $R - z' = 1.16$ line are those undetected in both R and z' . More than half (18/34) of the LAEs are invisible in z' . The red circles represent the spectroscopically confirmed LAEs ($N = 34$); open circles show that they are undetected in R ($N = 29$). The blue triangles and green crosses indicate nearby objects (19) and unclear objects (10), respectively. The yellow stars correspond to the 175 Galactic stars given in Gunn & Stryker's (1983) spectrophotometric atlas. The spectroscopically confirmed LAEs are found to be separate fairly well from the nearby objects. On the other hand, the unclear objects are located in a similar area to the LAEs; this may suggest that a significant fraction of the unclear objects are LAEs in reality.

The black solid curves show the tracks of model LAEs over a redshift range of $5.5 \leq z \leq 5.9$ with five different intrinsic EW values of Ly α in the rest frame: $W_0^i = 0$,

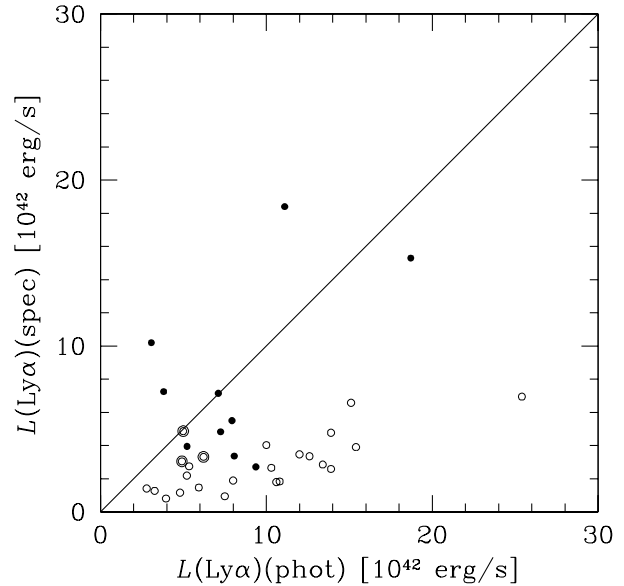


Fig. 6. Ly α luminosities measured from the spectra are plotted against those based on the photometric data for the 34 LAEs with spectroscopic confirmation. The filled and open circles indicate objects observed with DEIMOS and FOCAS, respectively. Three FOCAS objects observed through $0.8''$ slitlets are marked with large open circles.

20, 50, 150, and 300 Å from left to right; filled squares correspond to $z = 5.7$. In this paper, we assume that the intrinsic profile of Ly α emission is symmetric centered on zero velocity, and that foreground HI gas reduces intrinsic EWs 50% (blue half). Thus, we set the rest-frame apparent equivalent width after truncation by HI gas to be $W_0^a = 0.5 \times W_0^i$; the quantity measured from the data is W_0^a . Note that the assumption of 50% reduction has not been verified for LAEs at $z \sim 5.7$ and may be an oversimplification. As stated in Dawson et al. (2004), the dust content and detailed kinematics of the galaxy ISM appear to play a significant role in determining the emergent Ly α profile (e.g., Kunth et al. 1998; Stern & Spinrad 1999; Mas-Hesse et al. 2003; Shapley et al. 2003; Ahn 2004). LAEs at $z \sim 5.7$ may have a wide variety in the total absorption fraction of Ly α photons.

To calculate the model tracks, we construct the continuum spectral energy distribution of model galaxies using Kodama & Arimoto (1997) stellar population synthesis model, adopting a Salpeter IMF, a 10^7 yr age, and constant star formation. Note that LAEs without Ly α emission can have as red $i' - NB816$ colors as $\simeq 1.2$.

Based on this figure, we select $z = 5.7$ LAEs, by imposing the following four criteria on the NB816-detected

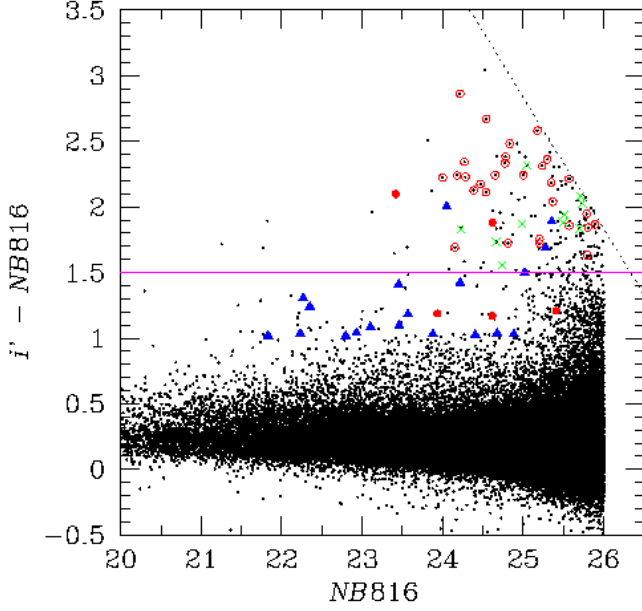


Fig. 7. $i' - \text{NB816}$ plotted against NB816 for objects with $\text{NB816} \leq 26.0$. The large symbols indicate objects with spectroscopic observations: red circles, blue triangles, and green crosses indicate LAEs ($N = 34$), nearby objects (19), and unclear objects (10), respectively. For LAEs, open circles mean R magnitudes fainter than the 2σ magnitude. The magenta line shows the threshold of $i' - \text{NB816}$ adopted for the selection of LAEs: $i' - \text{NB816} \geq 1.5$ (see text). The dotted line implies the i' -band 2σ limit.

multi-color catalog:

$$\text{NB816} \leq 26.0 \quad (\text{i})$$

$$i' - \text{NB816} \geq 1.5 \quad (\text{ii})$$

$$\{R - z' \geq 1.5 \text{ and } m_R < m_R(2\sigma)\} \text{ or } \{m_R \geq m_R(2\sigma)\} \quad (\text{iii})$$

$$m_B \geq m_B(2\sigma) \text{ and } m_V \geq m_V(2\sigma) \quad (\text{iv})$$

Objects satisfying these four criteria simultaneously are regarded as LAE candidates. The magenta solid lines in the figure indicate the selection boundary (in the case of $m_R < m_R(2\sigma)$) in the $R - z'$ vs $i' - \text{NB816}$ plane. In total 89 LAE candidates are selected, which we call the photometric sample.

Table 2 summarizes a breakdown of the spectroscopic sample ($N = 63$) in terms of the selection criteria for our photometric sample. Thirty-nine out of the 63 objects satisfy the photometric selection criteria for LAEs; 28 are confirmed LAEs, one is a nearby galaxy, and ten are unclassified. In the table, numbers in parentheses are the number of objects lying in the ‘high-quality’ region of 725 arcmin^2 used to construct the photometric sample of LAEs. Among the 28 confirmed LAEs, one is outside the ‘high-quality’ region, and thus is not included in the photometric sample. Thus, the 27 spectroscopically confirmed LAEs plus 62 photometrically selected candidates comprise our photometric sample of 89 LAEs. When discussing the $\text{Ly}\alpha$ equivalent-width distribution of the confirmed LAEs in subsection 5.2, we use the 28 LAEs which pass the photometric selection criteria. On

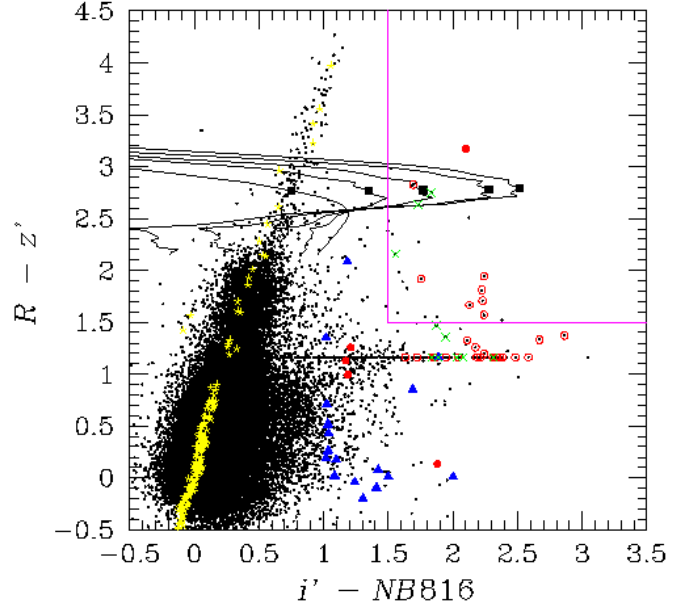


Fig. 8. Distribution of objects in the $R - z'$ vs $i' - \text{NB816}$ plane. The dots indicate objects with $\text{NB816} \leq 26.0$. If an object is undetected (i.e., fainter than the 2σ limit) in a given bandpass, its magnitude in that bandpass is replaced with the 2σ magnitude. Objects on the $R - z' = 1.16$ line are those undetected in both R and z' . The red circles represent the spectroscopically confirmed LAEs ($N = 34$); open circles show that they are undetected in R . The blue triangles and green crosses indicate nearby objects ($N = 19$) and unclear objects ($N = 10$), respectively. The yellow stars correspond to the 175 Galactic stars given in Gunn & Stryker's (1983) spectrophotometric atlas. The black solid curves show the tracks of model LAEs over a redshift range of $5.5 \leq z \leq 5.9$ with four different intrinsic EW values of $\text{Ly}\alpha$ in the rest frame: $W_0^i = 0, 20, 50, 150$, and 300 \AA from left to right; filled squares correspond to $z = 5.7$. The magenta solid lines indicate the selection boundary (in the case of $m_R < m_R(2\sigma)$).

the other hand, the contamination and completeness of the photometric sample are estimated using the 56 objects lying in the high-quality region.

The criterion of $i' - \text{NB816} \geq 1.5$ picks up LAEs with rest-frame equivalent widths of $W_0^i \gtrsim 20 \text{ \AA}$ (or $W_0^a \gtrsim 10 \text{ \AA}$). We adopt this criterion in order (i) not to select objects with very weak or no $\text{Ly}\alpha$ emission, and (ii) to avoid a high contamination by foreground objects whose $i' - \text{NB816}$ colors happen to exceed the criterion due to photometric errors. This lower limit to EWs in our selection is close to those set by Ajiki et al. (2003), $W_{\text{obs}} \geq 180 \text{ \AA}$ ($W_0 \geq 27 \text{ \AA}$), and by Rhoads & Malhotra (2001), $W_{\text{obs}} \geq 75 \text{ \AA}$ ($W_0 \geq 11 \text{ \AA}$). However, our lower limit to EWs is slightly higher than that used by Hu et al. (2004), $I - \text{NB816} \geq 0.7 - 1.0$ depending on the $R - z'$ color of the object. For LAEs at $z = 5.7$, Hu et al.'s criterion corresponds to $i' - \text{NB816} \gtrsim 1.1 - 1.4$. However, we find in our data that changing the criterion between $i' - \text{NB816} \geq 1.0$ and ≥ 1.5 does not significantly change the total number of candidates selected, if the selection is limited to objects brighter than $\text{NB816} = 25.5$; for objects fainter than this,

the contamination by foreground objects due to photometric errors is expected to be high at $i' - NB816 \leq 1.5$ (see Fig. 7), and thus we cannot make a reliable comparison of the number of LAEs. For $NB816 < 25.5$, the condition $i' - NB816 \geq 1.0$ leaves 66 objects while $i' - NB816 \geq 1.5$ selects 53. Considering that the $i' - NB816 \geq 1.0$ candidates will include a non-negligible fraction of foreground objects even at $NB816 < 25$, the difference in the number of true LAEs between the two $i' - NB816$ limits will be small.

We estimate the contamination and completeness of this photometric sample on the basis of the spectroscopic observations. The completeness of object detection, which is another completeness to be considered in calculating the LF, is discussed in the next section. As shown in Tab. 2, 56 out of the 63 objects with spectroscopic observation are from the region used to construct the photometric sample (725 arcmin^2). Among them, 36 satisfy the above criteria for LAE selection; 27 are LAEs, one nearby, and eight unclear objects. If all of the unclear objects are LAEs in reality, the contamination rate is calculated to be $1/36$. On the contrary, if all of the unclear objects are nearby objects, then the contamination is $(1 + 8)/36$. The average of these two extremes, 14%, is regarded as an estimate of contamination. The completeness is estimated as follows. Among the 56 spectroscopic objects lying in the region used to construct the photometric sample, 32 are confirmed LAEs and eight are unclear. Then, 27 out of the 32 LAEs and all eight unclear objects satisfy the photometric selection criteria for LAEs. Thus, the completeness is calculated as $(27 + 8)/(32 + 8)$ if all of the unclear objects are actually LAEs. It is reduced to $27/32$ if all of the unclear objects are nearby objects. The simple average of these two values is 86%.

These contamination and completeness estimates will not be so accurate, since the spectroscopic targets have not been chosen very uniformly in the two-color plane. When deriving the LFs of LAEs in the next section, we do not correct them for either completeness or contamination, because the completeness and contamination corrections using the values obtained above almost cancel; the combined factor is $(1 - 0.14)/0.86 = 1.00$.

5. Results and Discussion

In this section, we derive the Ly α LF and the far UV LF of $z = 5.7$ LAEs from the photometric sample, and examine the distribution of equivalent widths using the spectroscopic sample. The sky distribution of LAEs in the photometric and spectroscopic samples is also discussed.

5.1. Ly α Luminosity Function

5.1.1. Calculation of the Luminosity Function

Previous studies derived the Ly α LF by simply dividing the observed number counts of LAE candidates in a given narrow band by the effective survey volume defined as the FWHM of the bandpass times the area of the survey. Although this procedure is accurate when the narrow-band filter has an ideal, boxcar shape, the shapes

of actual filters used in LAE surveys are rather close to a triangle. In such cases, the narrow-band magnitude of LAEs of a fixed Ly α luminosity varies largely as a function of redshift. The selection function of LAEs in terms of equivalent width also changes with redshift; the minimum EW value corresponding to a given (fixed) narrow-band excess, such as $i' - NB816$, becomes larger when the redshift of the object goes away from the central redshift of the bandpass.

In order to avoid such uncertainties, we perform the following Monte Carlo simulations to find the best-fit Schechter parameters for the Ly α LF of $z = 5.7$ LAEs. First, we generate LAEs according to a given set of the Schechter parameters (α, ϕ^*, L^*) uniformly in comoving space over the redshift range $5.6 \leq z \leq 5.8$. Then, we ‘observe’ these LAEs in the NB816, R , i' , and z' bands, add to their flux densities photon noise corresponding to the actual observation, and select LAEs by the same criteria as for selecting the actual LAEs. Thus, we have a mock catalog of LAEs for the given set of (α, ϕ^*, L^*) . Finally, we compare the NB816-band number counts derived from the mock catalog with the observed counts, and compute the χ^2 value. By performing this set of simulations over a wide range of the Schechter parameters, we find the best-fit parameters.

Three points should be noted in these simulations. First, in the actual simulations we search for the best-fit ϕ^* and L^* values for only three values of α , $-1, -1.5, -2$, since the magnitude range of the observed number counts is not wide enough to place strong constraints on all three parameters simultaneously. These three α values are chosen following Malhotra & Rhoads (2004). The difference in χ^2 among the three α values is found to be insignificant, although $\alpha = -1$ gives the lowest χ^2 value. We adopt the $\alpha = -1.5$ results as the fiducial set of the best-fit Schechter parameters.

Second, in order to compute flux densities in the individual bandpasses from a given Ly α luminosity, we need to give an equivalent width. We assume a Gaussian distribution, $f(W_0^i) dW_0^i \propto \exp(-W_0^i{}^2/2\sigma_W^2) dW_0^i$, for the probability distribution of EWs for $z = 5.7$ LAEs, and generate objects by randomly sampling EWs from the $W_0^i > 0$ part of this distribution. The value of σ_W can be inferred from the observed $i' - NB816$ distribution and EW distribution. Figure 9 compares the predicted $i' - NB816$ distribution with the observation for four σ_W values: $\sigma_W = 50 \text{ \AA}$, 100 \AA , 200 \AA , and 400 \AA . For each prediction, $\alpha = -1.5$ and the best-fit L^* are used. It is found that $\sigma_W \approx 100 \text{ \AA}$ and 200 \AA are preferred among the four values. We then calculate the equivalent width distribution for $\sigma_W = 100 \text{ \AA}$ and 200 \AA , to find that the distribution for $\sigma_W = 200 \text{ \AA}$ is roughly consistent with the observed distribution of the spectroscopic sample, while that for $\sigma_W = 100 \text{ \AA}$ is much skewed toward lower EWs and thus clearly inconsistent with the observation. Based on these results, we decide to use $\sigma_W = 200 \text{ \AA}$ to find the best-fit Schechter parameters. We have confirmed that using $\sigma_W = 100 \text{ \AA}$ does not significantly change the best-fit parameters.

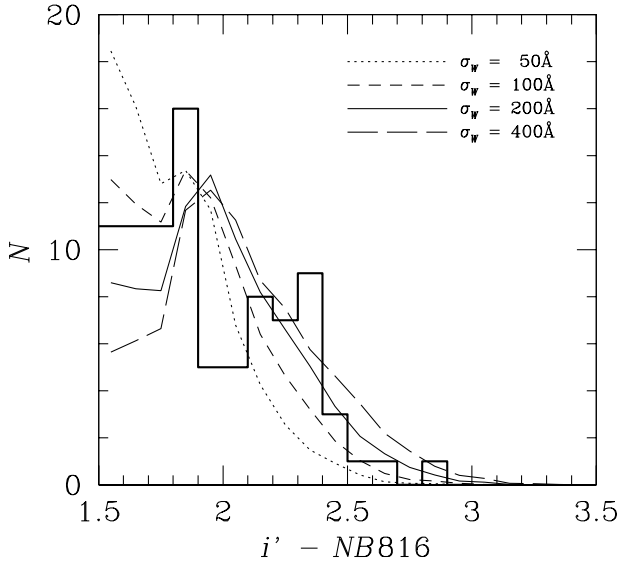


Fig. 9. Histogram of $i' - \text{NB816}$ for the photometric sample. The four curves indicate the predictions from simulations assuming four values for σ_W : $\sigma_W = 50, 100, 200, 400$ Å.

Third, we correct the observed number counts for detection completeness, since all objects are detected in the simulations irrespective of their magnitudes. We estimate the detection completeness as a function of apparent NB816 magnitude, by distributing pseudo objects on the NB816 image after adding photon noise, detecting them by SExtractor, and computing the detection fraction. We assume Gaussian profiles for pseudo objects whose size distribution (measured by SExtractor) matches that of the observed LAEs. The completeness thus computed is > 0.8 for $\text{NB816} < 25.0$, and is $\simeq 0.75$ at $\text{NB816} = 26.0$. The correction is thus modest in the whole magnitude range of the photometric sample.

We show in Figure 10 the observed number counts by circles and the predicted counts by three curves corresponding to the three α values. The dotted, solid, and dashed lines correspond to $\alpha = -1, -1.5$, and -2 , respectively. All three models reproduce the observed counts well, although shallower α gives a slightly better fit. This suggests that the Ly α LF of $z = 5.7$ LAEs is approximated well by the Schechter function. The best-fit parameters are $(L^* [\text{erg s}^{-1}], \phi^* [\text{Mpc}^{-3}]) = (5.2^{+1.4}_{-1.1} \times 10^{42}, 1.2^{+0.4}_{-0.3} \times 10^{-3})$, $(7.9^{+3.0}_{-2.2} \times 10^{42}, 6.3^{+3.0}_{-2.0} \times 10^{-4})$, $(1.6^{+0.9}_{-0.6} \times 10^{43}, 1.6^{+1.4}_{-0.7} \times 10^{-4})$ for $\alpha = -1, -1.5, -2.0$, respectively. The L^* values are ‘observed’ values. We assume that half of the intrinsic luminosities are erased due to

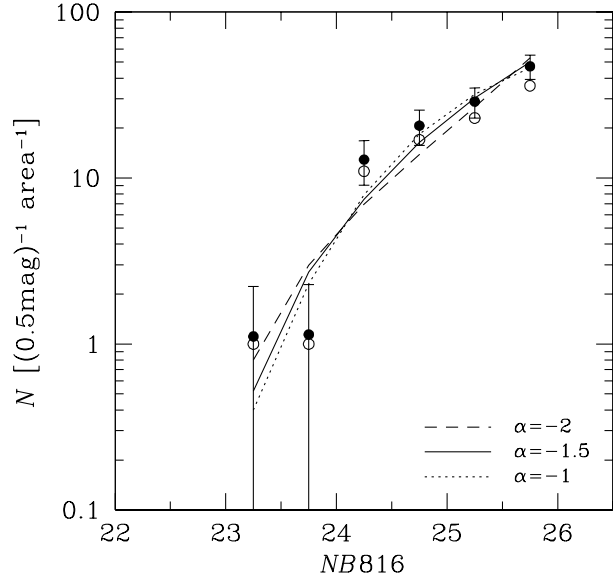


Fig. 10. Number counts of LAEs in the photometric sample. The filled circles represent the counts after correction for detection completeness, while the open circles show the raw counts. The dotted, solid, and dashed lines indicate, respectively, the best-fit Schechter functions for $\alpha = -1, -1.5$, and -2 derived in Subsection 5.1.

HI gas; one can thus double L^* to obtain intrinsic values.

The best-fit Schechter functions obtained above for $\alpha = -1, -1.5$, and -2 are shown in Figure 11 by the thick dotted, solid, and dashed lines, respectively. To give some idea about the luminosity range in which our Schechter functions are reliable, we plot a simple estimate of the luminosity function for our sample by the filled circles. These data points are obtained by dividing the number counts in NB816 (after correction for detection completeness) by the effective volume. Here, we calculate the Ly α luminosity of each object by subtracting the continuum emission measured from the z' -band magnitude from the total luminosity in the NB816 band, assuming $z = 5.7$. This is a rough estimate as described above, since NB816 magnitude for a given set of L and EW varies with redshift.

From Fig. 11, the Schechter functions are found to be reliable over $\approx 3 \times 10^{42} - 3 \times 10^{43} \text{ erg s}^{-1}$. In this range, the LFs for all three α values keep rising with decreasing L , suggesting that there exist many faint LAEs beyond our detection limit. Indeed, Santos et al. (2004) detected a high number density of faint ($L \sim 10^{40-42} \text{ erg s}^{-1}$) LAEs at $z = 4.5 - 5.7$ in a survey of lensed LAEs in very small areas. Malhotra & Rhoads (2004) found that a combination of

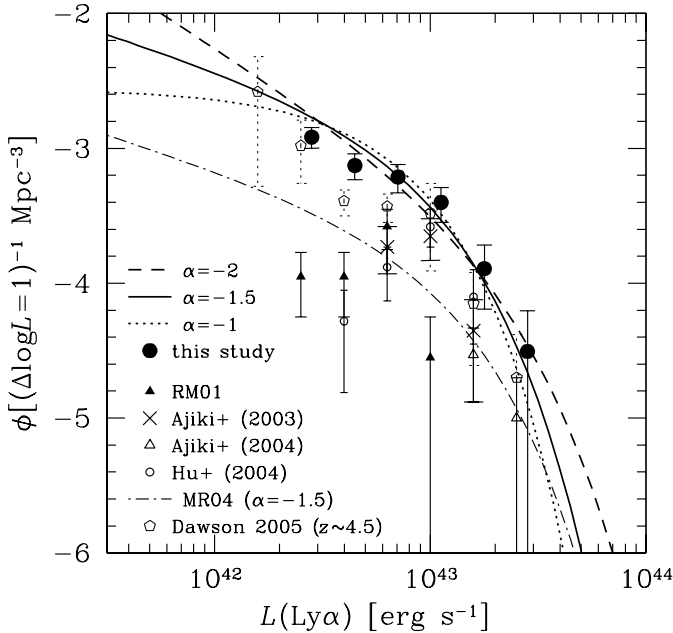


Fig. 11. Ly α luminosity functions of LAEs at $z = 5.7$. The dotted, solid, and dashed lines indicate, respectively, the best-fit Schechter functions for $\alpha = -1, -1.5$, and -2 derived in Subsection 5.1. The filled circles show rough estimates obtained by dividing the number counts of the photometric sample by the effective volume. The filled triangles, crosses, open triangles, and open circles indicate the data given by Rhoads & Malhotra (2001), Ajiki et al. (2003), Ajiki et al. (2004), and Hu et al. (2004). The dot-dashed line represents the luminosity function derived in Malhotra & Rhoads (2004) by fitting the Schechter function to a compiled data set. The pentagons represent the LF of LAEs at $z \sim 4.5$ by Dawson (2005).

Santos et al.’s LF with brighter estimates is consistent with Schechter functions of $\alpha \sim -1 - -2$.

Note that the simple estimate of the LF (filled circles) agrees fairly well with the best-fit Schechter functions. This means that the simple method gives a good approximation to the true LF at least for our data. This does not, however, reduce the importance of the accurate derivation of the LF made above, since we cannot judge the reliability of the simple estimate without an accurate calculation. In addition, the simulations used to derive the LF is useful in predicting the redshift distribution of LAEs in a flux-limited sample as well as placing a constraint on the distribution of EWs.

5.1.2. Comparison with Previous Measurements

Overplotted in Figure 11 are four previous results for $z = 5.7$ LAEs, which are taken from a compilation by Ajiki et al. (2004). The filled triangles represent the LF given in Rhoads & Malhotra (2001), which is based on a narrow-band sample of 18 candidates from a blank field of 710 arcmin². The crosses indicate the data in Ajiki et al. (2003) from 20 candidates detected in a 720 arcmin² area including the QSO SDSSp J104433.04–012522.2 at $z = 5.74$. The open triangles show the data in the same QSO field but from a survey with an intermediate-band filter (Ajiki et al. 2004). The open circles indicate Hu et al.’s (2004) measurements based on spectroscopically confirmed 19 LAEs in a blank field of 702 arcmin². The dot-dashed line denotes the LF given in Malhotra & Rhoads (2004) derived from a fit of the Schechter function to a compiled data set, including Rhoads & Malhotra (2001), Hu et al. (2004), and Ajiki et al. (2004). All but Ajiki et al. (2003) have not corrected for detection completeness.

At $L > 1 \times 10^{43}$ erg s⁻¹, our LF is in an acceptable agreement with those by Ajiki et al. (2003) and Hu et al. (2004). Ajiki et al.’s (2004) measurements are lower than ours, probably because they adopted a higher threshold for EWs, $W_0^a \gtrsim 45$ Å, than the other authors including us. At $L < 1 \times 10^{43}$ erg s⁻¹, our measurements are higher than all of the others by up to an order of magnitude. We infer that the main reason for this discrepancy is that our data are much deeper than the others and that the other measurements are not corrected for detection completeness. Large-scale inhomogeneity in the spatial distribution of LAEs may be another likely reason for the discrepancy. The differences in selection criteria for LAEs between our sample and the others are probably not a main reason for the discrepancy, since, for our data, changing the $i' - NB816$ threshold over 1.0 – 1.5 does not largely change the number of LAEs selected.

The open pentagons in Figure 11 represent the LF of $z \sim 4.5$ LAEs obtained by Dawson (2005) from 76 objects with spectroscopic redshifts. This LF is found to be slightly *lower* than our $z = 5.7$ LF, but the difference is within the 1σ errors for most data points. Thus, drastic evolution in the LAE LF from $z \sim 4.5$ to $z = 5.7$ is ruled out. Ouchi et al. (2003) show that the LF at $z = 4.9$ derived from a sample of 87 LAEs agrees with that for $z = 3.4$ LAEs by Cowie & Hu (1998), while Maier et al. (2003) found a significant decline in the LAE LF from $z = 3.4$ to $z = 5.7$ in their samples of $z = 4.8$ and $z = 5.7$. Our finding is consistent with Ouchi et al.’s (2003). The decrease found by Maier et al. (2003) could be due to the small statistics of their samples ($N = 5$ and 11 for $z = 4.8$ and 5.7), or an incompleteness in object detection in their relatively shallow data.

The largest uncertainty inherent in our LF measurements may be cosmic variance. The presence of large-scale structures of LAEs has been reported (Shimasaku et al. 2003, 2004; Ouchi et al. 2005). Hu et al. (2004) also found a highly structured distribution of LAEs at $z = 5.7$ in their $26.5' \times 26.5'$ field. Ouchi et al. (2005) used a catalog of $z = 5.7 \pm 0.05$ LAEs for a continuous 1

deg² area to calculate the rms fluctuation of LAE overdensity within a sphere of (comoving) 20 Mpc radius to be 40 ± 20 %. This is the estimate of the cosmic variance of LAEs on the largest scale reported so far. Our survey volume, 1.8×10^5 Mpc³, is five times larger than the volume of a sphere of 20 Mpc radius. Thus, the uncertainty in the number density of LAEs in our sample is likely to be much smaller than 40%, unless there exists an unusual inhomogeneity in the LAE distribution on scales of $\gg 20$ Mpc.

5.2. Equivalent Widths

5.2.1. Calculation of Equivalent Widths

We measure the rest-frame EWs of the spectroscopically confirmed 34 LAEs by two independent methods. The first method uses the z' -band magnitude to measure the continuum flux density, and calculates the EW by dividing the continuum-subtracted flux in NB816 by the flux density of the continuum. The second calculates the EW and the continuum flux density simultaneously from the i' and NB816 magnitudes. Note that at $z = 5.7$ the Ly α line enters both i' and NB816 bands. Malhotra & Rhoads (2002) used the first method, while Hu et al. (2004) applied both and then adopted the first method. In either method, we do not correct for the effect of H I absorption to the Ly α emission, while taking account of the IGM absorption of the continuum emission shortward of the Ly α line (Madau 1995). In what follows, $W_0^a(z')$ and $W_0^a(i')$ denote respectively the rest-frame EWs calculated from the first and the second methods.

The EW of the majority of our LAEs is highly uncertain because of their faint continuum emission; uncertainties are in general larger for objects with larger EWs. Furthermore, the probability distribution function of EW for each object, $P(W)dW$, is not symmetric but has a skewed shape with a long tail of large EWs, since the continuum emission enters into the denominator of the expression of EW. For each object and each of the above two methods, we carefully evaluate $P(W)$ using Monte Carlo simulations to calculate the central value of EW and its 1σ errors (see, e.g., Dawson et al. 2004). In the first method, we first assume that each flux density of NB816 and z' has a Gaussian probability density function centered on the measured flux density with a standard deviation of the measured error. Then we run Monte Carlo simulations to obtain a large set of (NB816, z') flux densities. Finally, we calculate EWs for individual (NB816, z') combinations of the set and derive $P(W)$. Similar simulations are performed for NB816 and i' in the second method.

The $W_0^a(z')$ and $W_0^a(i')$ values of the 34 LAEs derived above are given in Table 3. Three values in each of the $W_0^a(z')$ and $W_0^a(i')$ columns are the central value (W_c), 1σ lower limit (W_-), and 1σ upper limit (W_+) from left to right; they are defined as $\int_0^{W_c} P(W)dW = 0.5$ and $\int_{W_-}^{W_c} P(W)dW = \int_{W_c}^{W_+} P(W)dW = 0.34$. Figure 12 plots $W_0^a(i')$ against $W_0^a(z')$ (both are central values). The crosses correspond to the six objects with B or V detection; they are identical to the six objects not passing the

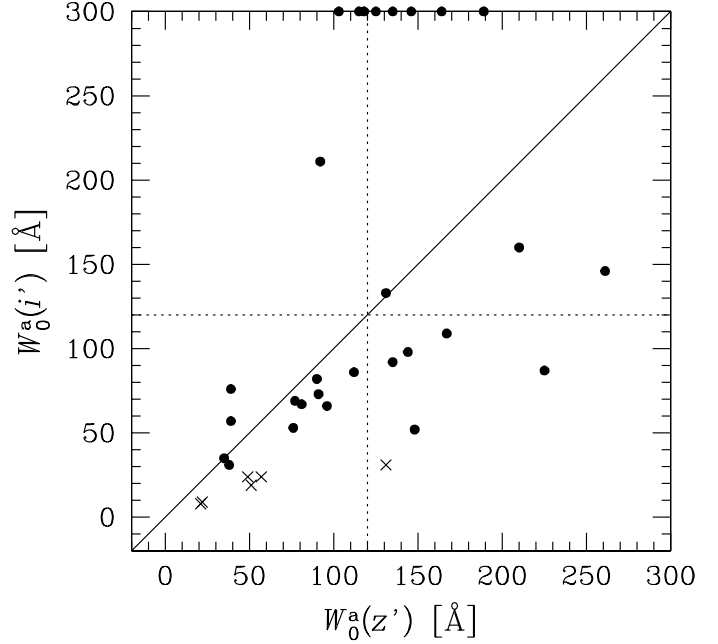


Fig. 12. $W_0^a(z')$ versus $W_0^a(i')$ for the 34 LAEs in the spectroscopic sample. The crosses indicate the six objects not meeting the photometric selection criteria for LAEs. The dotted lines indicate the maximum allowable value by normal star formation.

photometric selection criteria for LAEs. For low EW objects $W_0^a(i')$ correlates with $W_0^a(z')$, but little correlation is seen at $\gtrsim 100$ Å. Some objects with $W_0^a(z') \gtrsim 100$ Å have an extremely large $W_0^a(i')$. To derive $W_0^a(i')$, the continuum emission is calculated by subtracting the flux falling into the NB816 band from that falling into the i' band. Hence, the continuum emission calculated for objects with intrinsically faint continua (large EWs in most cases) can be close to zero or negative because of large photometric errors in i' -band magnitudes. Since a negative value is artificial and it actually means an extremely large (positive) EW, we assign $+\infty$ to objects with negative W_c .

The relative robustness against photometric errors between the two methods depends on the characteristics of the imaging data. We examine the reliability of $W_0^a(z')$ and $W_0^a(i')$ measurements using the simulations made to derive the Ly α LF in Subsection 5.1. Figure 13 plots $W_0^a(z')$ (panel [a]) and $W_0^a(i')$ (panel [b]) against the input value for 2,000 model LAEs randomly selected from the simulated objects which satisfy the selection criteria. The best-fit Schechter parameters for $\alpha = -1.5$ and $\sigma_W = 200$ Å are adopted. It is found that $W_0^a(z')$ shows a broad

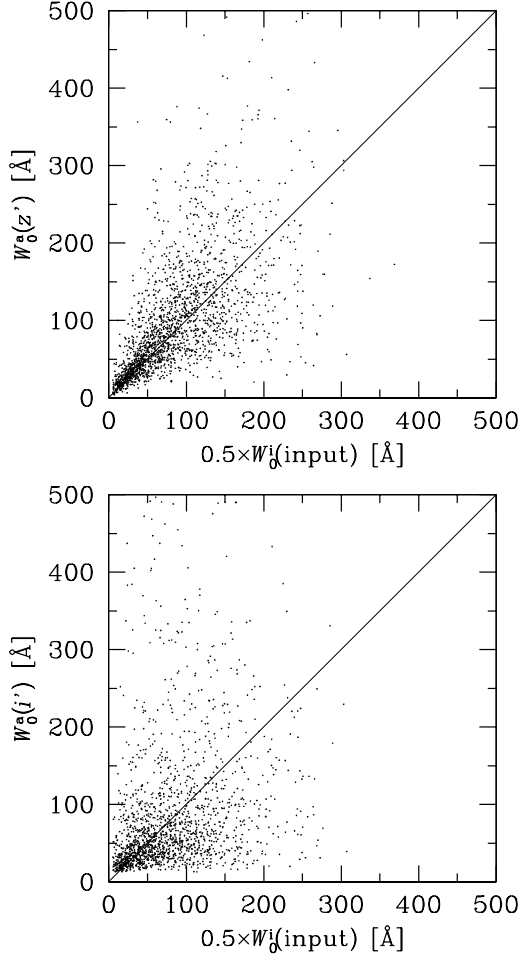


Fig. 13. Measured equivalent widths plotted against true (input) values for simulated LAEs. *Panel (a).* $W_0^a(z')$ versus $0.5 \times W_0^i(\text{input})$. *Panel (b).* $W_0^a(i')$ versus $0.5 \times W_0^i(\text{input})$. For both panels 2,000 objects are plotted. They are selected randomly from the simulated catalog with the best-fit Schechter parameters for $\alpha = -1.5$ and $\sigma_W = 200$ Å. All of the objects satisfy the selection criteria for LAEs.

but tighter correlation with the input value than $W_0^a(i')$. Panel (a) of Figure 14 presents the relative number distribution of the input and measured EW values for all simulated objects satisfying the selection criteria. The $W_0^a(z')$ distribution (dotted curve) agrees well with the input distribution (thin solid curve), while the $W_0^a(i')$ distribution (dashed curve) deviates largely in the sense that the number density of $W_0^a \sim 100 - 200$ Å objects is underestimated. Thus, we conclude that $W_0^a(z')$ is a more reliable measurement for our data. In what follows, we adopt $W_0^a(z')$ for the observed values.

We have inferred that the six objects detected either in B or V are contaminated by a foreground object. If this is the case, their equivalent widths derived from $NB816$ and z' photometry will be lower than the true values because of overestimated continuum emission (the effect on Ly α luminosity is little, as $NB816$ and z' flux densities are similarly contaminated). This underestimation of EWs

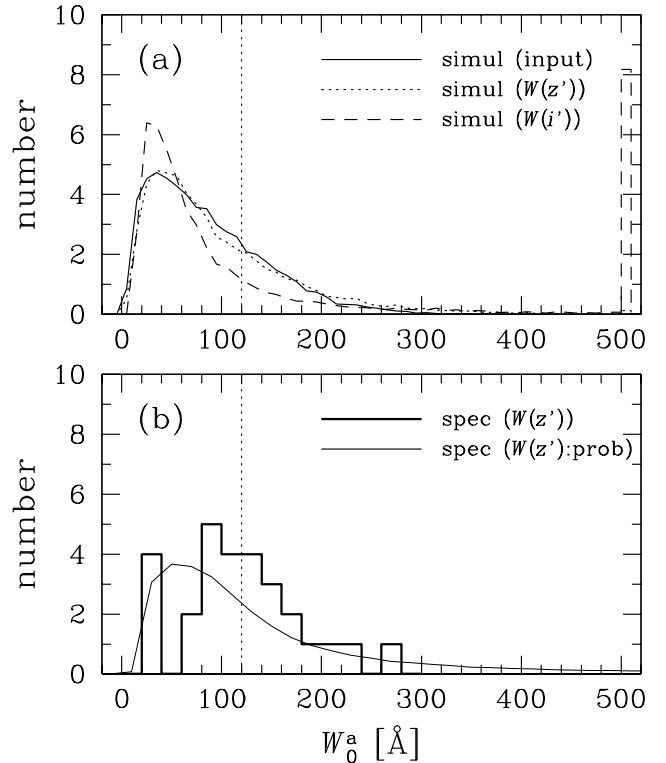


Fig. 14. *Panel (a).* Distributions of input and measured EW values for all simulated LAEs. The thin solid curve indicates the input (i.e., true) distribution. The dotted and dashed curves are for $W_0^a(z')$ and $W_0^a(i')$, respectively. For $W_0^a(i')$, objects with $W_0^a(i') \geq 500$ Å are shown at $W_0^a = 505$ Å. *Panel (b).* EW distribution of the 28 confirmed LAEs meeting the photometric selection criteria. The solid histogram represents the number frequency of $W_0^a(z')$ (central values), while the solid curve corresponds to the sum of their probability distribution functions ($P(W)$). In both panels, the dotted line indicates the maximum allowable value by normal star formation.

is, however, expected to be small, since (i) among the six objects three are detected in z' with both $B - z' > 1$ and $V - z' > 1$ and (ii) three are undetected in z' but two of them have B and V magnitudes very close to the detection limits. In addition, we do not use these six objects in the discussion of the EW distribution in the next subsection. Thus, we have not corrected their EW values for foreground contamination.

5.2.2. Equivalent Width Distribution

Figure 15 plots $W_0^a(z')$ against $L(\text{Ly}\alpha)$ for the 28 confirmed LAEs satisfying the photometric selection criteria. Objects shown by open circles have z' magnitudes fainter than the 1σ magnitude. The horizontal dotted line in Fig. 15 corresponds to a maximum value allowed by reasonable stellar populations ($W_0^i = 240$ Å) derived by Malhotra & Rhoads (2002). Continuously star-forming populations with population-I or -II metallicities assuming a Salpeter

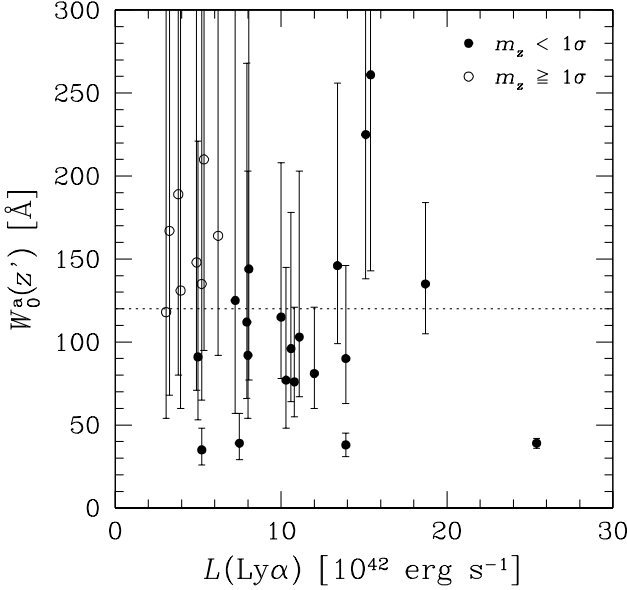


Fig. 15. $W_0^a(z')$ plotted against $\text{Ly}\alpha$ luminosity for the 28 confirmed LAEs which meet the photometric selection criteria. Objects shown by open circles have z' magnitudes fainter than the 1σ magnitude. The dotted line indicates the maximum allowable value by normal star formation.

mass function over the normal mass range cannot have EWs exceeding this value, unless they are as young as $\ll 1 \times 10^7$ yr (Charlot & Fall 1993; Malhotra & Rhoads 2002). The number frequency of $W_0^a(z')$ for the 28 LAEs is plotted in Figure 14 (b) by the solid histogram. The solid curve in Fig. 14 (b) corresponds to the sum of the probability distribution functions of the 28 objects.

Fig. 15 (and Fig. 14 [b]) shows that LAEs at $z = 5.7$ have very large EWs. The median $W_0^a(z')$ among the 28 objects is 117 Å (or $W_0^i(z') = 233$ Å), with lower and upper quartiles of 86 Å and 147 Å (171 Å and 294 Å in W_0^i), respectively. If the probability distribution function (solid curve in Fig. 14 (b)) is used, the median, lower quartile, and upper quartile are found to be $W_0^i(z') = 213, 125, 386$ Å, respectively. The EW distribution based on the spectroscopic sample will be biased toward large values, since the spectroscopic sample appears to be biased toward red $i' - \text{NB816}$ colors (i.e., large EWs). As an independent check, we calculate the median and quartiles from the best-fit simulations with $\sigma_W = 200$ Å, to find $W_0^i = 147$ Å (median), 80 Å (lower quartile), and 238 Å (upper quartile). Although smaller than the corresponding values from the spectroscopic sample, these values are still quite large.

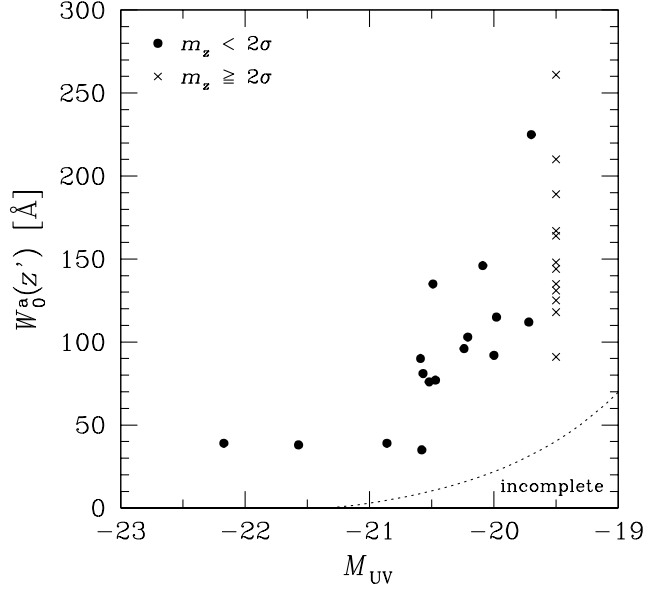


Fig. 16. Same as Fig. 15, but plotted against the far ultraviolet absolute magnitude, M_{UV} . See Subsection 5.3 for the calculation of M_{UV} . Objects fainter than the 2σ magnitude in z' are placed at $M_{\text{UV}} = -19.5$ and shown by crosses. The dotted curve indicates the lower limit of $W_0^a(z')$ detected in our sample ($z = 5.7$ is assumed for simplicity); objects below this curve are fainter than $\text{NB816} = 26.0$ and thus not included in our sample.

We do not find a significant correlation in $W_0^a(z')$ vs $L(\text{Ly}\alpha)$ (Fig. 15). However, we find that objects with fainter far-UV continuum luminosities tend to have larger EWs. Figure 16 plots $W_0^a(z')$ against far-UV absolute magnitude, M_{UV} , for the spectroscopic sample. See Subsection 5.3 for the calculation of M_{UV} . The dotted curve indicates the lower limit of $W_0^a(z')$ detected in our sample; objects below this curve are fainter than $\text{NB816} = 26.0$ and thus not included in our sample. It is found that all objects brighter than $M_{\text{UV}} = -20.7$ have $W_0^a(z') \leq 50$ Å. On the other hand, the majority of objects fainter than $M_{\text{UV}} = -20$ have $W_0^a(z') \geq 100$ Å unless a large number of objects exist below the dotted curve. If we interpret that objects with brighter M_{UV} are more massive, then the trend seen in Fig. 16 implies that less massive objects have larger EWs. Recently, Ando et al. (2005) obtained 11 spectra of $z \sim 5$ LBGs with $M_{\text{UV}} \lesssim -20.8$, finding that bright ($M \lesssim -21.5$) LBGs have EWs less than $W_0^a \simeq 20$ Å while the faintest two have large EWs of $W_0^a \simeq 40 - 80$ Å. This finding is very close to the trend seen in Fig. 16. It is also interesting to note that a

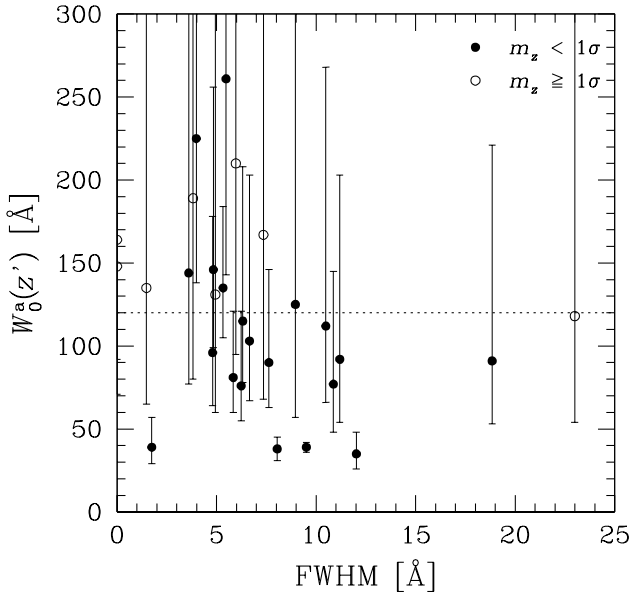


Fig. 17. Same as Fig. 15, but plotted against the FWHM of the Ly α line. The FWHM values have been corrected for spectral resolution. The dotted line indicates the maximum allowable value by normal star formation.

similar trend has been found for LBGs at $z \sim 3$ although their absolute EW values are much lower than our LAEs' (Shapley et al. 2003). We also find a weak, negative correlation between $W_0^a(z')$ and the FWHM of the Ly α line (Fig. 17). This is qualitatively consistent with the trend seen in Fig. 16, if the line width is due to Doppler broadening.

If one wants to reproduce the observed large median value by an ordinary, metal-enriched star-forming population with a Salpeter IMF (i.e., $x = 2.35$) of an upper mass cut of $120M_\odot$, one must assume very young ages ($< 1 \times 10^7$ yr), negligible dust extinction, and a nearly complete absorption of ionizing photons in the system (Kudritzki et al. 2000; Malhotra & Rhoads 2002). Such young ages mean that we are selectively picking up objects which have just started its star formation (or just entered a short star-formation phase if they have an episodic star-formation history). This leads us to an idea that there exist a much larger number of ancestors having not started star formation and descendants with ages since the onset of star formation too old to be selected as LAEs. This idea appears to be inconsistent with the observed far UV LF of LAEs and LBGs. In the next section we show that essentially

all $z \sim 6$ LBGs pass our selection criteria for LAEs. This implies that nearly half of LBGs have $W_0^i \gtrsim 200$ Å and thus younger than 1×10^7 yr. It looks unlikely that such a high fraction of LBGs fall into a so narrow range of age, since the LBG selection picks up star-forming galaxies irrespective of their ages as long as their apparent far UV flux densities are higher than a given detection limit. On the other hand, a small portion of our LAEs with equivalent widths lower than ~ 100 Å can be accounted for by ordinary Salpeter populations of reasonably old ages as long as dust extinction is negligible.

Other possibilities to account for the large median EW are top-heavy IMFs or zero-metallicity populations. Malhotra & Rhoads (2002) show that both an $x = 0.5$ IMF of 1/20 solar metallicity and a Salpeter IMF of zero metallicity can produce EWs $\gtrsim 200$ Å even if they are 10^8 yr or older, more than ten times older than the ages constrained for ordinary Salpeter populations. A special configuration of the interstellar medium (ISM) may also boost the equivalent width. Hansen & Oh (2005) argue that Ly α photons can preferentially escape from a dusty, multi-phase ISM than continuum photons if most of the dust is in cold neutral clouds, and thus that the EW of the transmitted spectrum can be larger than the EW of the unprocessed spectrum (see also Neufeld 1991). If this is the case, the observed large EWs can be reproduced by older (or steeper IMF slope) populations.

AGNs can also produce extremely large EWs. It is, however, unlikely that AGNs dominate in our sample, since our LAEs have very narrow rest-frame widths of the Ly α emission line, with a mean and rms of 1.07 Å and 0.68 Å, or 264 km s $^{-1}$ and 168 km s $^{-1}$ in velocity, after correction for spectral resolution. Recently, Wang et al. (2004) reported that no evidence of AGN activity (including low luminosity quasars) has been found for LAEs at $z \sim 4.5$ obtained from a narrow-band survey, either in deep X-ray data from *Chandra* or in optical spectra from Keck (see also Malhotra et al. 2003). Their report is consistent with our speculation, as we are probably selecting a similar population at $z = 5.7$ to their LAEs.

5.2.3. Objects Exceeding $W_0^i = 240$ Å

Objects with $W_0^i \geq 240$ Å are particularly interesting, since even a population of a very flat IMF of $x = 0.5$ (but metal enriched) cannot produce such large EWs unless it is younger than 1×10^7 yr (Malhotra & Rhoads 2002). We find in the confirmed 28 LAEs that 46 % (13 objects) have $W_0^i(z') \geq 240$ Å. Similarly, the fraction calculated from the probability distribution functions of EW is 44 %. We can also estimate the fraction from the simulations performed in subsection 5.1.1. The simulations for the best-fit Schechter parameters of the Ly α LF (for $\alpha = -1.5$ and $\sigma_W = 200$ Å) show that 24% of the objects satisfying the selection criteria have input values of $W_0^i \geq 240$ Å. Similarly, 29% of the objects satisfying the selection criteria have 'measured' values of $W_0^i(z') \geq 240$ Å. These values are lower than the observed values, 46 % and 44 %, probably reflecting the bias in $i' - NB816$ color in the spectroscopic target selection. Alternatively, the simula-

tions could underestimate the true fraction, since we have not been able to constrain σ_W so strongly.

From these results, we infer that the true fraction of $W_0^i \geq 240 \text{ \AA}$ is 30% – 40%. This value is much lower than that obtained by Malhotra & Rhoads (2002), 60%, from a photometric sample of $z = 4.5$ LAEs detected in their narrow-band survey. Our result may be closer to Hu et al.’s (2004); they found in their $z = 5.7$ LAE sample that the majority (11 out of 15 objects) have EWs less than 240 \AA , although they did not clearly present the fraction. The reason for the difference between our fraction and Malhotra & Rhoads’ is not clear. The evolutionary effect is unlikely, since it implies that the fraction of large-EW objects declines with redshift, which is opposite to the increasing fraction of strong Ly α emitters in LBGs (see the next subsection).

Recently, Dawson et al. (2004) obtained a more reliable fraction of large-EW objects for $z \sim 4.5$ LAEs from a sample of 17 objects with spectroscopic confirmation, but they calculated the fraction of $W_0^a > 240 \text{ \AA}$ in our definition, not $W_0^i > 240 \text{ \AA}$. Their calculation may be regarded as a conservative lower limit, since Ly α emission is assumed to be absorption free. Using the probability distribution function of EW from Monte Carlo simulations, they found with 90 % confidence that 18 – 29 % of LAEs in their sample exceed 240 \AA . A similar calculation for our 28 spectroscopic LAEs finds that 7 – 25 % exceed $W_0^a(z') = 240 \text{ \AA}$ with 90 % confidence. Thus, even without absorption correction, a certain fraction of $z = 5.7$ LAEs cannot be accounted for by normal star formation; the fraction is similar to that found for $z \sim 4.5$ LAEs. It is worth noting that in our sample we do not see evidence of large-EW objects being free from absorption. Among the six objects with $W_0^a > 150 \text{ \AA}$, at least five have a Ly α profile which shows clear asymmetry with a sharp cutoff in the blue side, suggesting a large amount of absorption.

5.3. Far-UV Luminosity Function

5.3.1. Calculation of the Luminosity Function

We derive the LF of the far UV continuum emission using the photometric sample of 89 LAE candidates. We transform the z' -band magnitude into the far UV continuum at the rest-frame 1350 \AA assuming that all of the LAEs are located at $z = 5.7$. For objects at $z = 5.7$, the z' band covers rest-frame wavelengths of $1250 \text{ \AA} - 1480 \text{ \AA}$ with a weighted center of 1350 \AA . Then the far UV LF is calculated by dividing the number of LAEs in each 0.5 magnitude bin by the effective volume corresponding to the FWHM of the NB816 bandpass ($1.80 \times 10^5 \text{ Mpc}^3$). In this calculation, the detection completeness in NB816 is taken into account. We do not convert the Ly α LF obtained in Subsection 5.1 into the far UV LF, since the conversion is sensitive to the EW distribution, which is still uncertain for our purpose here. For reference, the M_{UV} values of the 34 LAEs with spectroscopic redshifts are presented in Table 3.

Figure 18 plots the far UV LF obtained from our photometric sample by filled circles. The vertical dotted line at $M_{UV} = -19.58$ corresponds to the 2σ limiting mag-

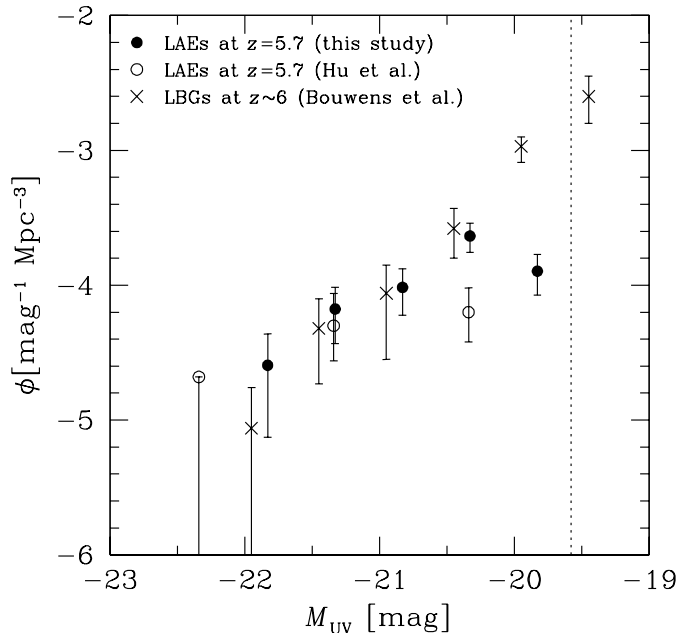


Fig. 18. Far ultraviolet ($\simeq 1350 \text{ \AA}$) luminosity functions of LAEs at $z = 5.7$ and LBGs at $z \sim 6$. The filled circles represent our measurements from the photometric sample. The vertical dotted line at $M_{UV} = -19.58$ corresponds to the 2σ limiting magnitude in the z' band; objects fainter than this magnitude have not been used. The open circles show the measurements by Hu et al. (2004). The crosses indicate the measurements for LBGs at $z \sim 6$ given in Bouwens et al. (2005).

tude in the z' band, 27.04 mag ; objects fainter than this magnitude have not been used to derive the LF. Note that our sample is not z' -magnitude limited but NB816-band limited ($NB816 \leq 26.0$). Since the scatter between z' and NB816 magnitudes is large, the detection completeness in terms of z' magnitude (or far UV magnitude) gradually drops when z' magnitude goes fainter because of undetection of objects with relatively fainter NB816 magnitudes (for a given z' magnitude). We find, from the plot of apparent z' magnitude versus NB816 magnitude, that the measurement of the far UV LF is incomplete to some degree at M_{UV} fainter than ~ -20.5 . Therefore, the apparent flattening of the LF at $M_{UV} > -20.5$ seen in Figure 18 may be partly due to this incompleteness. The open circles show the far UV LF of $z = 5.7$ LAEs obtained by Hu et al. (2004). Their measurements agree with ours very well at $M_{UV} < -21$, but their value at $M_{UV} = -20.3$ is lower than ours by a factor of four, probably reflecting the detection incompleteness of their sample.

5.3.2. $Ly\alpha$ Emission of LBGs

We compare the far UV LF of our LAEs with that of $z \sim 6$ LBGs. Determinations of the far UV LF of $z \sim 6$ LBGs have been recently accumulating (e.g., Dickinson et al. 2004; Yan & Windhorst 2004; Bunker et al. 2004; Bouwens et al. 2005; Shimasaku et al. 2005); see a compilation given in Bouwens et al. (2005). The differences in $\phi(M)$ among the determinations are roughly within a factor of three. We adopt here Bouwens et al.'s (2005) results (crosses in Fig. 18), since they are based on a very large sample of 506 LBGs from several deep surveys including the GOODS fields and the Hubble Ultra Deep Field (HUDF), and since their results are in the middle among the previous determinations.

LBGs at $z \sim 6$ are detected as i' -dropout galaxies in multi-color broad-band surveys, and thus they include all galaxies with far UV continua brighter than a lower limit defined by the survey depth. In Fig. 18, the LAE LF is found to be comparable to the LBG LF over the whole magnitude range examined, except for our data point at the faintest magnitude. As stated above, the data point at the faintest magnitude probably suffers from a large incompleteness, and thus the true difference from the LBG LF will be smaller. We can thus conclude that at $z \sim 6$ nearly all of far-UV selected galaxies with $M_{UV} \lesssim -20$ have a strong $Ly\alpha$ emission with $W_0^i \geq 20 \text{ \AA}$. In other words, an LAE survey like ours can pick out essentially all galaxies brighter than $M_{UV} \sim -20$ at $z \sim 6$.

Malhotra et al. (2005) compared the far UV LF of $z \sim 6$ LBGs in the HUDF with the $Ly\alpha$ LF of $z = 5.7$ LAEs given in Malhotra & Rhoads (2002), to find similar ϕ^* values (after correction for an overdensity seen in the HUDF LBGs). They argue that the LBG space density could be consistent with that of LAEs, but they could not compare the space densities of these two populations in a common far UV absolute magnitude range. We demonstrate in this study that the space densities of LBGs and LAEs at $z \sim 6$ are similar at least down to $M_{UV} \sim -20$.

Figure 18 may suggest that the majority of $z \sim 6$ LBGs have dust-free, extremely young ages and/or top-heavy IMFs, if we recall that our LAEs have extremely large EWs. A recent observation of far UV colors of i' -dropout galaxies (i.e., $z \sim 6$ LBGs) by Stanway et al. (2005) shows steep (i.e., blue) UV slopes, which might suggest young ages ($\sim 10^7$ yr) or top-heavy IMFs, although their sample is limited to faint objects ($M_{UV} > -20$) and thus does not overlap with our sample. On the other hand, *Spitzer Space Telescope* observations of bright ($M_{UV} \lesssim -21$) i' -dropout galaxies (LBGs at $z \sim 6$) give old ages of a few $\times 10^8$ yr and large stellar masses of a few $\times 10^{10} M_\odot$ (Yan et al. 2005; Eyles et al. 2005; see also Mobasher et al. 2005 for the finding of a J -dropout galaxy at $z \sim 6.5$ with an old age and an extremely large stellar mass). *Spitzer* observations of HCM 6A (spectroscopically confirmed, $Ly\alpha$ emitting galaxy at $z = 6.56$ behind Abell 370) give very young ages of an order of 10^6 yr (Chary, Stern, & Eisenhardt 2005), but this object is fainter than -21 .

It is also suggested that bright LBGs have small EWs; Bunker et al. (2003) and Stanway et al. (2004) made

spectroscopy of six $z \sim 6$ LBGs with $M_{UV} \lesssim -21$, finding that two have $W_0^a = 20 - 30 \text{ \AA}$ and the rest have no detectable $Ly\alpha$ emission (A similar trend was found for $z \sim 5$ LBGs by Ando et al. 2005). This supports our finding that LAEs with brighter M_{UV} have on average smaller EWs (Fig. 16). These results collectively suggest that there is a large variety in the star formation history in $z \sim 6$ galaxies depending on their mass; massive galaxies are considerably evolved while low-mass galaxies tend to be very young.

Our study reveals that LBGs at $z \sim 6$ have much larger EWs than those at $z \sim 3$. Steidel et al. (2000) and Shapley et al. (2003) found that 20 – 25% of bright ($M_{UV} < -20$) LBGs at $z \sim 3$ have $W_0^i \geq 20 \text{ \AA}$ (Their measurements include $Ly\alpha$ absorption). This value is a factor 4 – 5 lower than that obtained above for $z \sim 6$ LBGs, since almost all $z \sim 6$ LBGs pass our LAE selection, $W_0^i \gtrsim 20 \text{ \AA}$. Moreover, the fraction of LBGs with $W_0^i \geq 100 \text{ \AA}$ is $\sim 2\%$ at $z \sim 3$ (Shapley et al. 2003), but this fraction rises to as high as about 80% at $z \sim 6$, since 24 out of the 28 spectroscopic LAEs have $W_0^i \geq 100 \text{ \AA}$ (The probability distribution functions of the 28 LAEs give 82%). Our finding of high fractions of large-EW LBGs is qualitatively consistent with the recent finding by Nagao et al. (2005); they found that at least three out of 48 i' -dropout galaxies at $z \sim 6$ have $W_0^i \geq 200 \text{ \AA}$.

The extremely high fraction of large-EW LBGs at $z \sim 6$ suggests strong evolution of $Ly\alpha$ properties of far-UV selected star-forming galaxies over $z \sim 6$ and $z \sim 3$. The origin of this evolution cannot be specified in this study, but possible candidates will include lower dust extinction, younger stellar ages, and drastic changes in metallicity and the IMF slope toward lower and flatter values, respectively, with increasing redshift. The increase in the fraction of large EW objects with redshift seems qualitatively in accord with the recent finding that the far UV continuum of LBGs is on the average bluer at $z \sim 6$ than at $z \sim 3$ (Bouwens et al. 2005; Stanway et al. 2005).

We calculate the star formation rate for the 89 LAE candidates from the far-UV absolute magnitude using the formula given in Madau et al. (1998). This formula has been applied to LBGs and LAEs at various redshifts in previous studies. Our calculation is limited to the objects brighter than $M_{UV} = -19.58$. The star formation rates span $\simeq 4 - 40 M_\odot \text{ yr}^{-1}$. By dividing the sum of the star formation rates by the survey volume, we obtain the star formation rate density to be $2.3 \times 10^{-3} M_\odot \text{ yr}^{-1} \text{ Mpc}^{-3}$. This value is twice as high as the estimate given by Ajiki et al. (2003), reflecting the deeper limiting magnitude of our data, and thus is regarded as a new lower limit of the far-UV based star formation rate density in the $z \sim 6$ universe from LAE surveys. Our value is about one third that derived from the LF of $z \sim 6$ LBGs (i' -dropout galaxies) down to $0.3L_{z=3}^*$ (or -19.6 mag) by Bouwens et al. (2005), $\simeq 6 \times 10^{-3} M_\odot \text{ yr}^{-1} \text{ Mpc}^{-3}$.

Note, however, that the formula used above to convert M_{UV} into star-formation rate, given in Madau et al. (1998), assumes a constant star formation of solar metal-

licity with a Salpeter IMF of ages of $\gg 10^7$ yr. Thus, this formula cannot be applied to our LAEs if they have very young ($< 10^7$ yr) ages or top-heavy IMFs or zero metallicity as suggested from the large EW values. The star formation rate will be underestimated by this formula for very young populations, while it will be overestimated for populations with top-heavy IMFs. Therefore, while we can robustly conclude that LAEs have a significant contribution to the total far-UV luminosity density in the $z \sim 6$ universe, the star formation rate density itself could contain a large systematic error. Furthermore, recalling that nearly all LBGs at $z \sim 6$ have EWs large enough to be selected as LAEs, we suspect that the star-formation rate density measurements for LBGs may also suffer from a similar uncertainty.

5.3.3. $\text{Ly}\alpha$ Bias for the LF of $z \sim 6$ LBGs

Finally, let us discuss an interesting implication of the large EWs of $z \sim 6$ LBGs for their far UV LF. In most cases, LBGs at $z \sim 6$ were selected from their red $i' - z'$ colors, and their M_{UV} magnitudes were calculated from z' -band photometry (An important exception is the work by Shimasaku et al. 2005). At $z = 6$, however, the redshifted $\text{Ly}\alpha$ line is located around the peak transmission of the z' band. In what follows we take the F850LP band of ACS as a typical z' band. If an LBG at $z \sim 6$ has $W_0^i = 200$ Å, then its F850LP-band magnitude will be about 0.8 mag brighter than the value expected in the case of no $\text{Ly}\alpha$ emission, since its observed-frame equivalent width will be as large as 1300 Å (exact values depending on redshift), which is nearly the same as the FWHM of the F850LP band. This simple calculation implies that the far-UV LF of $z \sim 6$ LBGs calculated from z' -band magnitudes will be biased toward higher luminosities. This bias is stronger for fainter LBGs, since fainter LBGs have larger EWs on average (Fig. 16). Comparing the LF at $z \sim 6$ with those at lower redshifts will require correction to the former for this bias. The correction not only will strengthen the recent finding that the number density of bright LBGs drops from $z \sim 3$ to $z \sim 6$ (e.g., Ouchi et al. 2004; Shimasaku et al. 2005; Bouwens et al. 2005), but also might find a new trend that faint LBGs also decrease in number toward $z \sim 6$. Nagao et al. (2004, 2005) have also argued significant brightening of z' -band magnitudes of i' -dropout galaxies due to large EWs.

5.4. Spatial Distribution

The sky distribution of our LAEs is shown in Figure 19. The small dots indicate the 89 candidates in the photometric sample. The open circles and crosses represent, respectively, 34 LAEs in the spectroscopic sample with $z \leq 5.7$ and $z > 5.7$. The thick solid lines outline the region used to make the photometric sample. Some spectroscopic objects do not have a counterpart in the photometric sample because they are either out of the region used to construct the photometric sample, or ruled out by the selection criteria.

A large-scale density contrast is seen in the sky distribution of the 89 candidates. The average surface num-

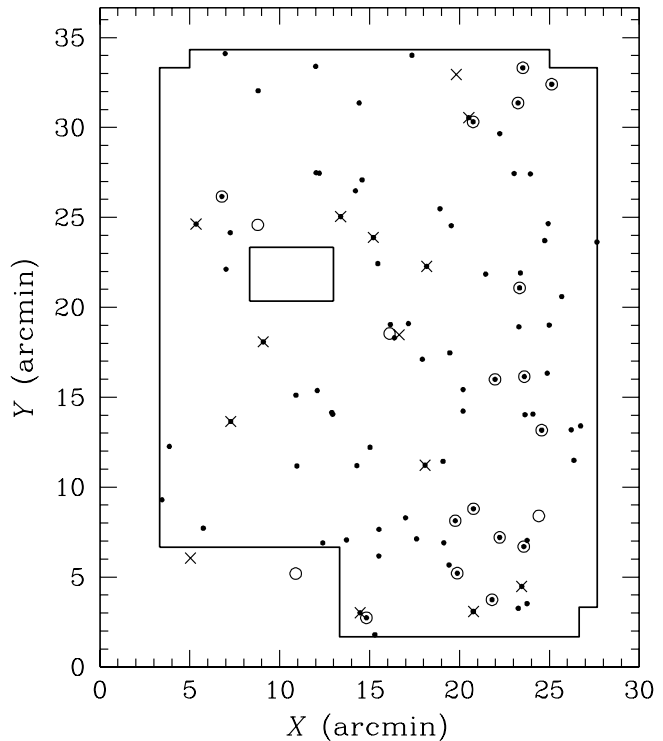


Fig. 19. Sky distribution of the LAEs in the photometric and spectroscopic samples. The small dots indicate the 89 candidates in the photometric sample. The open circles and crosses represent, respectively, 34 LAEs in the spectroscopic sample with $z \leq 5.7$ and $z > 5.7$. The thick solid lines outline the region used to make the photometric sample.

ber density over the whole region is $0.12 \pm 0.01 \text{ arcmin}^{-2}$. When the whole region is split into two at $X = 17'$, the surface number density is $0.097 \pm 0.016 \text{ arcmin}^{-2}$ for the eastern half and $0.15 \pm 0.02 \text{ arcmin}^{-2}$ for the western half; these values differ from the average about $\pm 20\%$. The line-of-sight distribution of the spectroscopic sample also shows inhomogeneity. Objects with $z \leq 5.7$ dominate in the western half, while those with $z > 5.7$ dominate in the eastern half. These findings collectively suggest the existence of large-scale structure in our sample.

Figure 20 plots the angular correlation function for the photometric sample (filled circles). Clustering signals are found not to be significant; the large-scale inhomogeneity found above is not strong enough to be clearly reflected in angular correlation. We also calculate the angular correlation for a bright subsample of $\text{NB816} \leq 25.5$ (open circles), since brighter galaxies are in general known to be clustered more strongly at high redshift as well, but we do not see significant clustering. We, however, find possible clustering of the $\sim 2\sigma$ level at a very small separation of $< 10''$ in the angular correlation function, which might

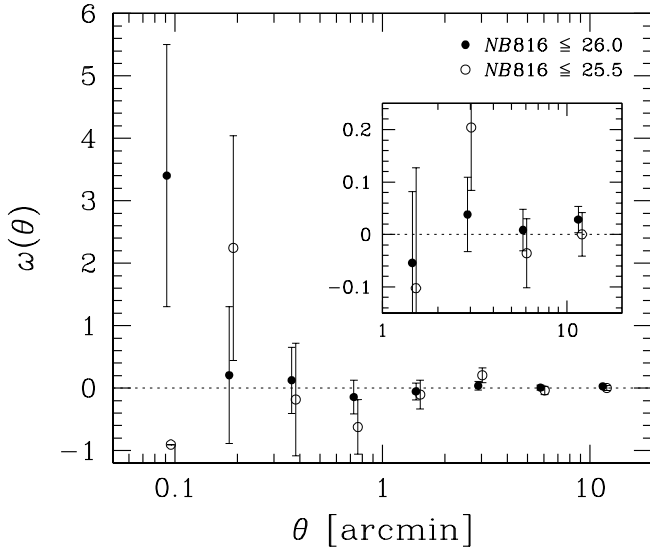


Fig. 20. Angular correlation function of LAEs in the photometric sample. The filled and open circles correspond to the whole sample ($N = 89$) and a bright ($NB816 \leq 25.5$) sample ($N = 53$), respectively. The inset shows an expanded view at $\theta \geq 1'$. The data points have been shifted to the horizontal direction by -0.01 and $+0.01$ for the whole and bright samples, respectively, for clarity.

suggest that LAEs tend to form close pairs.

Ouchi et al. (2005) have examined the sky distribution of $z = 5.7$ LAEs in a 1 deg^2 area, about five times larger than our survey area, and found filamentary large-scale structures on scales of several tens of Mpc. The large-scale structure found in our sample appears not to be as prominent as the filamentary structures of Ouchi et al. sample. A similar observation has been obtained for $z \simeq 4.8$ LAEs by Shimasaku et al. (2003, 2004). They have surveyed for LAEs in $z = 4.79 \pm 0.04$ and $z = 4.86 \pm 0.03$ slices of the universe in a $25' \times 45'$ area of the SDF, and found a large-scale structure in the latter slice, while finding no angular clustering in the former slice.

6. Summary

We have presented the results of a deep survey of Ly α emitters (LAEs) at $z = 5.7$ in the Subaru Deep Field. A total of 89 LAE candidates with $NB816 \leq 26.0$ were selected from imaging data of six bandpasses, including the narrow band NB816, taken with Suprime-Cam on Subaru. These candidates have $i' - NB816 \geq 1.5$, red $R - z'$ colors,

and B and V fluxes fainter than the 2σ limits. Spectra of 39 objects satisfying the photometric selection criteria for LAEs were obtained with FOCAS on Subaru and DEIMOS on Keck II. The spectroscopic classification of objects was made using weighted skewness, which quantifies the asymmetry of the emission line. Among the 39 objects, 28 are confirmed LAEs, one is a nearby galaxy, and eight are unclassified. Among the 28 confirmed LAEs, one is outside the region used to construct the photometric sample of LAEs. Also obtained were spectra of another 24 NB816-excess objects in the field; six are LAEs and 18 are nearby galaxies. We have thus 34 confirmed LAEs in total. The spectroscopic results show that the photometric sample of 89 LAEs is highly reliable with a low contamination.

Using these photometric and spectroscopic samples of LAEs, we have studied the LFs, the equivalent width distribution, and the spatial distribution of LAEs at $z = 5.7$. We summarize the main results below.

- By generating mock catalogs of LAEs, we have searched for the Schechter parameters of the Ly α LF of $z = 5.7$ LAEs which best fit the observed number counts in the NB816 band. We have found $(L^* [\text{erg s}^{-1}], \phi^* [\text{Mpc}^{-3}]) = (5.2^{+1.4}_{-1.1} \times 10^{42}, 1.2^{+0.4}_{-0.3} \times 10^{-3})$, $(7.9^{+3.0}_{-2.2} \times 10^{42}, 6.3^{+3.0}_{-2.0} \times 10^{-4})$, $(1.6^{+0.9}_{-0.6} \times 10^{43}, 1.6^{+1.4}_{-0.7} \times 10^{-4})$ for $\alpha = -1, -1.5, -2.0$, respectively, over the range where our data are available, $L \simeq 3 \times 10^{42} - 3 \times 10^{43} \text{ erg s}^{-1}$. The Ly α LF of $z = 5.7$ LAEs is reproduced well by the Schechter function. Our LF is consistent with the previous measurements at $L > 1 \times 10^{43} \text{ erg s}^{-1}$ within the errors, but largely overshoots them at $L < 1 \times 10^{43} \text{ erg s}^{-1}$, probably reflecting the detection incompleteness of the previous surveys. No significant evolution is found in the LF between $z \sim 4.5$ and $z = 5.7$.
- We have measured rest-frame Ly α equivalent widths for the spectroscopically confirmed LAEs. We have found that the median value among the 28 LAEs satisfying the photometric selection criteria is $W_0^i = 233 \text{ \AA}$, with lower and upper quartiles of 171 \AA and 294 \AA , respectively, where W_0^i , which we regard as the intrinsic value, is twice the measured value. About 30% – 40% of LAEs at $z = 5.7$ are inferred to exceed $W_0^i = 240 \text{ \AA}$, from both the spectroscopic sample and the simulations. LAEs with $W_0^i \gtrsim 200 \text{ \AA}$ are unlikely to be accounted for by metal enriched, continuously star-forming populations with a Salpeter IMF; metal-free populations or top-heavy IMFs are required. We have also found that LAEs with fainter far-UV magnitudes have larger EWs.
- We have derived the far-UV ($\simeq 1350 \text{ \AA}$) LF for LAEs at $z = 5.7$ down to $M_{\text{UV}} \simeq -19.6$ from the photometric sample. We have found that this LF agrees with the far-UV LF of LBGs at similar redshifts over the whole magnitude range where the completeness of our sample is expected to be relatively high. This implies that at $z \sim 6$ almost all star-forming galaxies brighter than $M_{\text{UV}} \sim -20$ have

Ly α emission strong enough to be detected as LAEs ($W_0^i \geq 20$ Å). Moreover, the fraction of $z \sim 6$ LBGs with $W_0^i \geq 100$ Å is found to be about 80%. These extremely high fractions are in sharp contrast to lower-redshift LBGs, suggesting drastic evolution in Ly α emission properties. We have also argued that the far-UV LF and the star formation rates of star-forming galaxies at $z \sim 6$ measured from z' -band photometry could contain large systematic errors.

- We have found large-scale structure in the spatial distribution of our sample both in the tangential and radial directions, although it is not as prominent as the filamentary structures seen in Ouchi et al.'s (2005) much larger survey for $z = 5.7$ LAEs.

We thank an anonymous referee for valuable comments which have much improved the paper. We are grateful to the staff of the Subaru and Keck Telescopes. This research would not be made possible without the unique and excellent data obtained for the Subaru Deep Field Project. We deeply thank all members of the project who are not co-authors of this paper. N.K. acknowledges support by the Japan Society for the Promotion of Science through Grant-in-Aid for Scientific Research 16740118. M.O. has been supported by the Hubble Fellowship program through grant HF-01176.01-A awarded by the Space Telescope Science Institute, which is operated by the Association of Universities for Research in Astronomy, Inc. under NASA contract NAS 5-26555.

References

- Ahn, S. 2004, *ApJ*, 601, L25
 Ajiki, M. et al. 2003, *AJ*, 126, 2091
 Ajiki, M. et al. 2004, *PASJ*, 56, 597
 Ando, M., Ohta, K., Iwata, I., Akiyama, M., Aoki, K., & Tamura, N. 2005, in ‘The Fabulous Destiny of Galaxies: Bridging Past and Present’ (Marseille, France) (astro-ph/0510830)
 Bertin, E., & Arnouts, S. 1996, *A&AS*, 117, 393
 Bouwens, R. J. et al. 2005, *ApJ*, submitted (astro-ph/0509641)
 Bunker, A. J., Stanway, E. R., Ellis, R. S., & McMahon, R. G. 2004, *MNRAS*, 355, 374
 Bunker, A. J., Stanway, E. R., Ellis, R. S., McMahon, R. G., & McCarthy, P. J. 2003, *MNRAS*, 342, L47
 Charlot, S. & Fall, S. M. 1993, *ApJ*, 415, 580
 Chary, R., Stern, D. & Eisenhardt, P. 2005, *ApJ*, 635, L5
 Cowie, L. L. & Hu, E. M. 1998, *AJ*, 115, 1319
 Dawson, S. 2005, Ph. D thesis, University of California, Berkeley
 Dawson, S. et al. 2004, *ApJ*, 617, 707
 Dickinson, M. et al. 2004, *ApJ*, 600, L99
 Eyles, L. P. et al. 2005, *MNRAS*, in press (astro-ph/0502385)
 Faber, S. M. et al. 2003, *Proc. SPIE*, 4841, 1657
 Gunn, J. E., & Stryker, L. L. 1983, *ApJS*, 52, 121
 Haiman, Z. 2002, *ApJ*, 576, L1
 Haiman, Z. & Spaans, M. 1999, *ApJ*, 518, 138
 Haiman, Z., Spaans, M., & Quataert, E. 2000, *ApJ*, 537, L5
 Hansen, M. & Oh, S. P. 2005, *MNRAS*, submitted (astro-ph/0507586)
 Hu, E. M., Cowie, L. L., McMahon, R. G., Capak, P., Iwamuro, F., Kneib, J.-P., Maihara, T., & Motohara, K. 2002, *ApJ*, 568, L75 (erratum 576, L99 [2002])
 Hu, E. M., Cowie, L. L., Capak, P., McMahon, R. G., Hayashino, T., & Komiyama, Y. 2004, *AJ*, 127, 563
 Iye, M. et al. 2004, *PASJ*, 56, 381
 Kashikawa, N. et al. 2002, *PASJ*, 54, 819
 Kashikawa, N. et al. 2004, *PASJ*, 56, 1011
 Kashikawa, N. et al. 2005, submitted to *ApJ*
 Kodaira, K. et al. 2003, *PASJ*, 55, L17
 Kodama, T., & Arimoto, N. 1997, *A&A*, 320, 41
 Kudritzki, R.-P. et al. 2000, *ApJ*, 536, 19
 Kunth, D., Mas-Hesse, J. M., Terlevich, E., Terlevich, R., Lequeux, J., & Fall, S. M. 1998, *A&A*, 334, 11
 Kurk, J. D. et al. 2004, *A&A*, 422, L13
 Madau, P. 1995, *ApJ*, 441, 18
 Madau, P., Pozzetti, L., & Dickinson, M. 1998, *ApJ*, 498, 106
 Maier, C. et al. 2003, *A&A*, 402, 79
 Maihara, T. et al. 2001, *PASJ*, 53, 25
 Malhotra, S. et al. 2005, *ApJ*, 626, 666
 Malhotra, S., Wang, J. X., Rhoads, J. E., Heckman, T. M., & Norman, C. A. 2003, *ApJ*, 585, L25
 Malhotra, S., & Rhoads, J. E. 2002, *ApJ*, 565, L71
 Malhotra, S., & Rhoads, J. E. 2004, *ApJ*, 617, L5
 Mas-Hesse, J. M., Kunth, D., Tenorio-Tagle, G., Leitherer, C., Terlevich, R. J., & Terlevich, E. 2003, *ApJ*, 598, 858
 Miyazaki, S., et al. 2002, *PASJ*, 54, 833
 Mobasher, B. et al. 2005, *ApJ*, 635, 832
 Nagao, T. et al. 2004, *ApJ*, 613, L9
 Nagao, T. et al. 2005, *ApJ*, in press
 Neufeld, D. A. 1991, *ApJ*, 370, L85
 Ouchi, M. et al. 2003, *ApJ*, 582, 60
 Ouchi, M. et al. 2004, *ApJ*, 611, 660
 Ouchi, M. et al. 2005, *ApJ*, 620, L1
 Rhoads, J. E., & Malhotra, S. 2001, *ApJ*, 563, L5
 Rhoads, J. E. et al. 2003, *AJ*, 125, 1006
 Santos, M. R., Ellis, R. S., Kneib, J.-P., Richard, J., & Kuijken, K. 2004, *ApJ*, 606, 683
 Schlegel, D. J., Finkbeiner, D. P., & Davis, M. 1998, *ApJ*, 500, 525
 Shapley, A. E., Steidel, C. C., Pettini, M., & Adelberger, K. L. 2003, *ApJ*, 588, 65
 Shimasaku, K. et al. 2003, *ApJ*, 586, L111
 Shimasaku, K. et al. 2004, *ApJ*, 605, L93
 Shimasaku, K. et al. 2005, *PASJ*, 57, 447
 Stanway, E. R., Bunker, A. J., McMahon, R. G., Ellis, R. S., Treu, T., & McCarthy, P. J. 2004, *ApJ*, 607, 704
 Stanway, E. R., McMahon, R. G., & Bunker, A. J. 2005, *MNRAS*, 359, 1184
 Stern, D. et al. 2005, *ApJ*, 619, 12
 Stern, D. & Spinrad, H. 1999, *PASP*, 111, 1475
 Steidel, C. C., Adelberger, K. L., Shapley, A. E., Pettini, M., Dickinson, M., & Giavalisco, M. 2000, *ApJ*, 532, 170
 Taniguchi, Y. et al. 2005, *PASJ*, 57, 165
 Wang, J. X. et al. 2004, *ApJ*, 608, L21
 Yan, H. et al. 2005, *ApJ*, in press (astro-ph/0507673)
 Yan, H. & Windhorst, R. A. 2004, *ApJ*, 612, L93

Table 1. Spectroscopic properties

(a) LAEs														
ID	α (J2000.0)	δ (J2000.0)	z	I	S_W	NB816	B	V	R	i'	z'	$i' - \text{NB816}$	$R - z'$	
(1)	(2)	(3)	(4)	(5)	(6)	(7)	(8)	(9)	(10)	(11)	(12)	(13)	(14)	
18699	13 24 38.94	+27 13 40.9	5.645	D	5.03 ± 0.82	25.80	28.8	28.1	28.20	27.84	27.04	1.84	1.16	
20087	13 24 40.52	+27 13 57.9	5.724	D	8.18 ± 0.23	24.00	28.8	28.1	28.20	26.48	26.39	2.22	1.81	
20495	13 24 11.88	+27 14 2.0	5.697	D	7.03 ± 0.41	24.77	28.8	28.1	28.20	27.52	27.04	2.33	1.16	
23759	13 24 7.20	+27 14 41.6	5.687	F	5.81 ± 5.16	24.65	28.8	28.1	28.20	27.40	26.26	2.24	1.94	
27787	13 23 59.71	+27 15 26.3	5.707	F	6.03 ± 2.25	25.23	28.8	28.1	28.20	27.84	27.04	2.31	1.16	
31858	13 24 56.80	+27 16 9.7	5.692	D	6.01 ± 0.88	25.57	28.8	28.1	28.20	27.84	27.04	2.21	1.16	
31765	13 24 15.99	+27 16 11.1	5.691	F	5.90 ± 2.52	24.38	28.8	28.1	28.20	26.96	26.53	2.13	1.67	
36334	13 25 23.41	+27 17 1.3	5.705	D	3.75 ± 0.43	24.62	27.6	26.9	26.47	25.93	25.34	1.17	1.13	
39849	13 23 59.17	+27 17 40.7	5.692	F	4.85 ± 1.14	24.21	28.8	28.1	28.20	27.38	26.82	2.86	1.37	
42576	13 24 5.27	+27 18 11.6	5.684	F	6.30 ± 0.98	24.54	28.8	28.1	28.20	27.45	26.87	2.67	1.33	
46904	13 24 16.47	+27 19 7.7	5.665	F	10.30 ± 1.65	24.15	28.8	28.1	28.20	26.18	25.37	1.69	2.83	
48328	13 23 55.36	+27 19 23.7	5.693	F	7.28 ± 4.88	25.80	28.7	28.1	28.20	27.49	27.04	1.63	1.16	
50215	13 24 11.87	+27 19 48.2	5.682	F	6.48 ± 1.94	25.30	28.8	28.1	28.20	27.84	27.04	2.36	1.16	
61418	13 24 24.11	+27 22 15.1	5.748	D	8.00 ± 0.01	25.00	28.8	28.1	28.20	27.83	27.00	2.24	1.20	
70600	13 23 54.60	+27 24 12.7	5.654	F	8.77 ± 0.80	24.81	28.8	28.1	28.20	26.70	27.04	1.72	1.16	
73078	13 25 13.27	+27 24 42.0	5.700	D	11.62 ± 2.14	25.79	28.8	28.1	28.20	27.84	27.04	1.95	1.16	
84305	13 24 6.39	+27 27 4.2	5.695	F	8.38 ± 1.84	24.28	28.8	28.1	28.20	26.96	26.49	2.23	1.71	
84720	13 23 58.98	+27 27 13.4	5.682	F	20.66 ± 6.02	24.47	28.8	28.1	28.20	27.45	26.94	2.17	1.26	
93966	13 25 5.06	+27 29 10.3	5.721	F	5.36 ± 3.74	25.18	28.8	28.1	28.20	27.84	27.04	2.58	1.16	
95588	13 24 30.63	+27 29 34.5	5.738	F	8.60 ± 4.55	25.41	28.3	28.1	28.05	26.93	26.79	1.21	1.26	
96007	13 24 33.09	+27 29 38.6	5.696	F	6.28 ± 5.63	25.20	28.7	28.1	28.20	27.47	27.04	1.72	1.16	
108164	13 24 0.15	+27 32 12.1	5.672	F	4.13 ± 2.23	25.89	28.8	28.1	28.20	27.84	27.04	1.87	1.16	
113271	13 24 23.70	+27 33 24.8	5.710	F	11.82 ± 1.01	23.41	28.8	28.1	27.91	25.80	24.73	2.10	3.17	
121315	13 24 37.19	+27 35 2.3	5.716	F	3.38 ± 2.33	25.37	28.8	28.1	28.20	27.77	27.04	2.04	1.16	
124530	13 25 6.48	+27 35 44.5	5.689	D	3.33 ± 0.19	24.62	27.4	27.5	27.17	27.01	27.04	1.88	0.13	
124783	13 25 22.12	+27 35 46.8	5.720	D	7.66 ± 0.80	25.20	28.8	28.1	28.20	27.20	26.28	1.75	1.92	
126848	13 24 45.48	+27 36 12.6	5.718	F	10.49 ± 6.73	25.35	28.8	28.1	28.20	27.71	27.04	2.19	1.16	
132343	13 25 15.60	+27 37 19.9	5.697	D	6.28 ± 0.83	24.78	28.8	28.1	28.20	27.61	27.04	2.38	1.16	
152586	13 24 11.89	+27 41 31.8	5.681	F	6.11 ± 1.64	24.18	28.8	28.1	28.20	27.03	26.63	2.24	1.57	
154296	13 24 13.00	+27 41 45.8	5.715	F	5.01 ± 2.76	25.57	28.8	28.1	28.20	27.84	27.04	1.86	1.16	
158036	13 24 0.51	+27 42 35.3	5.676	F	12.68 ± 1.53	24.83	28.8	28.1	28.20	27.84	27.04	2.48	1.16	
163079	13 23 51.96	+27 43 38.2	5.676	F	4.38 ± 1.21	24.54	28.8	28.1	28.20	27.16	26.87	2.11	1.33	
166310	13 24 16.13	+27 44 11.6	5.698	F	10.61 ± 1.80	23.93	26.1	25.9	25.83	25.43	24.84	1.19	0.99	
168127	13 23 59.27	+27 44 33.8	5.674	F	6.28 ± 0.78	24.27	28.8	28.1	28.20	27.06	27.04	2.34	1.16	
(b) nearby objects														
ID	α (J2000.0)	δ (J2000.0)	z	I	S_W	NB816	B	V	R	i'	z'	$i' - \text{NB816}$	$R - z'$	
28247	13 24 11.70	+27 15 30.5	...	F	2.99 ± 0.30	24.05	27.0	26.9	26.83	26.21	26.82	2.00	0.01	
29275	13 25 17.89	+27 15 46.4	...	D	-6.40 ± 0.12	22.79	25.8	25.4	24.87	24.35	23.52	1.02	1.35	
31925	13 25 15.61	+27 16 11.0	1.182	D	-8.49 ± 0.20	24.40	26.4	26.1	25.88	25.62	25.17	1.02	0.71	
34775	13 25 8.10	+27 16 48.1	...	D	0.14 ± 0.19	23.57	28.1	27.4	26.60	25.55	24.52	1.18	2.08	
38133	13 23 56.28	+27 17 26.1	1.180	F	-1.88 ± 0.05	22.23	24.0	23.8	23.73	23.51	23.21	1.03	0.52	
42561	13 24 3.41	+27 18 17.8	0.630	F	0.65 ± 0.01	21.83	24.1	23.8	23.41	23.14	23.22	1.02	0.19	
56181	13 25 25.87	+27 21 12.0	0.620	D	1.68 ± 0.23	24.88	27.5	27.4	26.79	26.23	26.54	1.03	0.25	
59788	13 25 10.24	+27 21 53.2	0.628	D	1.34 ± 0.14	25.02	27.8	28.0	27.05	26.68	27.04	1.50	0.01	
68251	13 23 40.67	+27 23 45.6	0.635	D	1.44 ± 0.00	23.46	25.8	25.6	25.04	24.73	24.87	1.10	0.17	
70071	13 24 34.91	+27 24 10.2	0.623	D	0.26 ± 0.00	22.35	24.6	24.4	24.04	23.77	24.08	1.24	-0.04	
76702	13 24 5.75	+27 25 37.3	1.186	D	-5.99 ± 0.00	22.93	24.6	24.4	24.39	24.17	23.96	1.04	0.43	
78892	13 24 15.26	+27 25 60.0	0.615	F	-0.23 ± 0.01	23.10	25.8	25.6	24.95	24.42	24.93	1.08	0.02	
96705	13 24 25.59	+27 29 47.2	0.632	F	2.92 ± 0.67	25.27	28.5	27.9	27.89	27.04	27.04	1.69	0.85	
99588	13 23 57.78	+27 30 30.1	0.636	F	-1.82 ± 0.43	24.21	26.9	26.8	26.41	25.99	26.34	1.42	0.08	
110439	13 25 24.72	+27 32 44.3	0.629	D	0.06 ± 0.00	23.45	25.9	25.8	25.36	24.99	25.46	1.41	-0.10	
122518	13 25 13.45	+27 35 17.9	1.174	D	-1.03 ± 0.00	25.35	28.8	28.1	28.20	27.84	27.04	1.89	1.16	
136295	13 25 5.54	+27 38 10.0	0.244	D	-3.23 ± 0.01	22.27	24.2	24.0	23.69	23.71	23.89	1.30	-0.20	
165225	13 24 53.38	+27 43 57.7	0.637	D	-13.95 ± 0.77	24.67	27.0	26.7	26.10	25.81	25.83	1.04	0.26	
168136	13 24 3.01	+27 44 34.7	...	F	-3.69 ± 0.33	23.88	25.5	25.4	25.30	25.09	24.79	1.03	0.51	

(c) unclear objects														
ID	α (J2000.0)	δ (J2000.0)	z	I	S_W	NB816	B	V	R	i'	z'	$i' - \text{NB816}$	$R - z'$	
17721	13 25	9.51 +27 13 29.4	...	D	2.93 ± 0.53	24.67	28.8	28.1	28.09	26.81	25.45	1.73	2.63	
34503	13 25	7.24 +27 16 38.7	...	D	0.92 ± 1.30	25.50	28.8	28.1	28.20	27.84	26.84	1.94	1.36	
41967	13 23	58.35 +27 18 1.4	...	F	0.01 ± 0.28	25.73	28.8	28.1	28.20	27.84	27.04	2.03	1.16	
74901	13 23	58.83 +27 25 5.1	...	F	-2.86 ± 2.14	25.49	28.8	28.1	28.20	27.49	27.04	1.88	1.16	
89624	13 24	24.80 +27 28 11.9	...	F	2.04 ± 0.97	25.70	28.8	28.1	28.20	27.84	27.04	1.84	1.16	
91179	13 24	17.84 +27 28 33.4	...	F	2.20 ± 0.92	25.05	28.8	28.1	28.20	27.84	27.04	2.32	1.16	
97631	13 24	0.34 +27 30 1.0	...	F	2.01 ± 1.40	24.98	28.8	28.1	28.20	27.16	26.73	1.87	1.47	
98040	13 24	32.88 +27 30 8.8	...	F	-6.53 ± 2.32	24.22	28.8	28.1	28.20	26.44	25.45	1.83	2.75	
105644	13 23	49.49 +27 31 42.7	...	F	-0.13 ± 0.80	24.74	28.8	28.1	28.20	27.05	26.04	1.56	2.16	
111685	13 24	8.75 +27 32 58.8	...	F	-0.60 ± 0.25	25.70	28.8	28.1	28.20	27.84	27.04	2.08	1.16	

Notes.

(1): ID in the NB816-detected catalog.

(4): Redshift. For LAEs 1215.67 Å is adopted as the Ly α wavelength.

(5): Instrument used. D = DEIMOS, F = FOCAS. The nearby object 76702 was observed with FOCAS as well. We have adopted the DEIMOS spectrum with a better spectral resolution.

(6): Weighted skewness.

(7) – (12): Magnitudes in the six bandpasses. NB816 magnitude is the MAG_AUTO magnitude, and the others are 2''-aperture magnitudes. Magnitudes fainter than the 2σ magnitudes have been replaced with the 2σ magnitudes.

(13),(14): Colors measured on a 2'' aperture.

Table 2. Breakdown of the spectroscopic sample in terms of the selection criteria for our photometric sample

class	selection criteria		total
	satisfy	not satisfy	
LAE	28 (27)	6 (5)	34 (32)
nearby	1 (1)	18 (15)	19 (16)
unclear	10 (8)	0 (0)	10 (8)
total	39 (36)	24 (20)	63 (56)

Notes.

Numbers in parentheses are the number of objects lying in the region used to construct the photometric sample of LAEs (See Fig. 19 and section 4).

Table 3. Ly α and continuum properties of confirmed LAEs

ID	z	FWHM	$L(\text{Ly}\alpha)^{\text{sp}}$	$L(\text{Ly}\alpha)$	$W_0^a(z')$			$W_0^a(i')$			M_{UV}	SFR
(1)	(2)	(3)	(4)	(5)	(6)			(7)			(8)	(9)
18699	5.645	9.0	4.8	7.2 ± 3.6	125	57	329	∞	∞	∞
20087	5.724	5.3	15.3	18.7 ± 0.7	135	105	184	92	67	139	-20.49	8.5
20495	5.697	10.5	5.5	7.9 ± 1.0	112	66	268	86	40	780	-19.72	4.2
23759	5.687	1.8	0.9	7.5 ± 1.1	39	29	57	76	37	364	-20.86	11.9
27787	5.707	6.0	2.8	5.3 ± 0.9	210	95	701	160	47	∞
31858	5.692	3.8	7.2	3.8 ± 0.9	189	80	618	3321	63	∞
31765	5.691	6.2	1.8	10.8 ± 1.1	76	55	121	53	33	104	-20.52	8.8
36334	5.705	4.8	7.2	7.1 ± 0.9	22	19	26	9	7	12	-21.42	20.0
39849	5.692	4.8	2.9	13.4 ± 0.9	146	99	256	1478	170	∞	-20.09	5.9
42576	5.684	6.3	4.0	10.0 ± 1.0	115	78	208	409	102	∞	-19.98	5.3
46904	5.665	8.1	4.8	13.9 ± 1.7	38	31	45	31	21	48	-21.57	23.1
48328	5.693	0.6	1.4	2.8 ± 0.9	51	27	120	19	8	60
50215	5.682	1.5	2.2	5.2 ± 1.0	135	65	421	∞	86	∞
61418	5.748	6.7	18.4	11.1 ± 1.1	103	67	203	354	94	∞	-20.21	6.5
70600	5.654	4.0	6.6	15.1 ± 2.3	225	138	487	87	34	482	-19.70	4.1
73078	5.700	23.0	10.2	3.1 ± 0.9	118	54	378	∞	85	∞
84305	5.695	5.8	3.5	12.0 ± 1.1	81	60	121	67	42	143	-20.57	9.1
84720	5.682	10.9	2.7	10.3 ± 1.4	77	48	145	69	32	289	-20.47	8.4
93966	5.721	0.0	3.3	6.2 ± 0.8	164	92	475	∞	183	∞
95588	5.738	6.8	1.5	5.9 ± 0.9	57	40	100	24	16	37	-20.14	6.2
96007	5.696	6.1	1.2	4.8 ± 1.1	49	29	108	24	11	61	-20.08	5.8
108164	5.672	7.3	1.3	3.3 ± 1.3	167	68	635	109	21	∞
113271	5.710	9.5	7.0	25.4 ± 0.8	39	36	42	57	49	67	-22.17	40.1
121315	5.716	0.0	3.0	4.9 ± 0.8	148	71	505	52	26	276
124530	5.689	2.2	2.7	9.4 ± 1.1	131	78	307	31	20	61	-19.65	3.9
124783	5.720	12.0	4.0	5.2 ± 0.8	35	26	48	35	22	65	-20.58	9.2
126848	5.718	18.8	4.9	5.0 ± 0.8	91	53	221	73	33	592
132343	5.697	3.6	3.4	8.1 ± 1.0	144	77	387	98	43	∞
152586	5.681	7.6	2.6	13.9 ± 1.3	90	63	146	82	45	197	-20.59	9.3
154296	5.715	4.9	0.8	4.0 ± 0.9	131	60	431	133	35	∞
158036	5.676	11.2	1.9	8.0 ± 1.4	92	54	203	211	52	∞	-20.00	5.4
163079	5.676	4.8	1.8	10.6 ± 1.4	96	64	178	66	35	193	-20.24	6.8
166310	5.698	9.3	3.4	12.6 ± 0.9	21	19	24	8	6	9	-22.08	36.7
168127	5.674	5.5	3.9	15.4 ± 1.4	261	143	656	146	69	1423

Notes.

(1): ID in the NB816-detected catalog. Shown in bold font are objects not satisfying the photometric selection criteria.

(2): redshift.

(3): FWHM of the Ly α line in the observed frame (\AA).(4): Ly α luminosity ($\times 10^{42} \text{ erg s}^{-1}$) calculated from the spectrum.(5): Ly α luminosity ($\times 10^{42} \text{ erg s}^{-1}$) calculated from the NB816- and z' -band photometry combined with the spectroscopic redshift.(6): $W_0^a(z')$ (\AA). The first, second, and third columns are the central value (W_c), 1σ lower limit (W_-), and 1σ upper limit (W_+). These values are defined as $\int_0^{W_c} P(W)dW = 0.5$ and $\int_{W_-}^{W_c} P(W)dW = \int_{W_c}^{W_+} P(W)dW = 0.34$, where $P(W)dW$ is the probability distribution of EW derived from Monte Carlo simulations.(7): $W_0^a(i')$ (\AA). The first, second, and third columns are the central value, 1σ lower limit, and 1σ upper limit. The definition of these values is the same as for $W_0^a(z')$.

(8): Far-UV continuum absolute magnitude (AB).

(9): Star formation rate calculated from M_{UV} ($M_{\odot} \text{ yr}^{-1}$).